In situ produced cosmogenic krypton in zircon and its potential for Earth surface applications

Tibor János Dunai [1*], Steven Andrew Binnie[1], Axel Gerdes[2]

[1] Institute of Geology and Mineralogy, University of Cologne, Zülpicher Str. 49b, 50674 Cologne, Germany.

[2] Institute for Geosciences, Goethe-University Frankfurt, Altenhöferallee 1, 60438 Frankfurt am Main, Germany.

Correspondence to: Tibor J. Dunai (tdunai@uni-koeln.de)

Abstract

Analysis of cosmogenic nuclides produced in surface rocks and sediments is a valuable tool for assessing rates of processes and the timing of events that shaped the Earth surface. The various nuclides that are used have specific advantages and limitations that depend on the time-range over which they are useful, the type of material they are produced in, and not least the feasibility of the analytical effort. Anticipating novel applications in Earth surface sciences, we develop in-situ produced terrestrial cosmogenic krypton (Kr_{it}) as a new tool; the motivation being the availability of six stable and one radioactive isotope (^{81}Kr, half-life 229 kyr) and of an extremely weathering-resistant target mineral (zircon). We provide proof of principle that terrestrial Kr_{it} can be quantified and used to unravel Earth surface processes.

1 Introduction

Cosmogenic nuclides have become an important tool to address questions in Earth surface sciences and paleoclimatology (Dunai, 2010; Gosse and Phillips, 2001; Balco, 2020). These nuclides are produced by particles of the cosmic ray cascade in the atmosphere and in minerals (i.e., in situ) at or close to the Earth's surface (Dunai, 2010; Gosse and Phillips, 2001). Each of the currently applied in situ produced cosmogenic nuclides, i.e., ^{3}He, ^{10}Be, ^{14}C, ^{21}Ne, ^{26}Al, ^{36}Cl, and ^{53}Mn, has specific benefits and limitations that are rooted in its half-life, or stability in the case of ^{3}He and ^{21}Ne, the availability of suitable target minerals and our ability to measure the exceedingly low amounts produced (typically between 1-100 atoms per gram per year at sea level (Dunai, 2010)). In space, production rates are at least three orders of magnitude higher than on Earth at ground-level. Hence, many in situ produced nuclides were initially developed in studies of extra-terrestrial material (e.g., meteorites, lunar rocks) some thirty years before they began to be used to transform quantitative Earth surface sciences. Cosmogenic krypton, $^{78,80-86}Kr$ (Marti et al., 1966; Gilabert et al., 2002; Marti, 1967) has not made this transition yet, despite having the potential. Krypton is the only noble gas that has stable ($^{78,80,82-84,86}Kr$) and short-lived radioactive

isotopes (^{81,85}Kr) that are produced by cosmic rays (Gilabert et al., 2002; Marti et al., 1966). An exception is cosmogenic argon (^{36,37,38,39}Ar; (Renne et al., 2001; Niedermann et al., 2007; Saldanha et al., 2019), which, due to inherent limitations (Renne et al., 2001; Dunai, 2010), still awaits widespread application to Earth surface sciences (Oostingh et al., 2017).With a half-life ($t_{1/2}$) of 229 ± 11 kyr (Baglin, 2008), ^{81}Kr is particularly attractive for geomorphological applications, however, only the cosmogenic ^{81}Kr produced in the atmosphere has been used in Earth sciences to date, as a dating tool for old ice and groundwater (Buizert et al., 2014; Sturchio et al., 2004).

1.1 In situ produced *extra*-terrestrial krypton

In situ produced extra-terrestrial krypton, Kr_{iet}, in meteorites has been measured for over fifty years (Marti et al., 1966; Marti, 1967). For instance, the Kr-Kr dating method of meteorites (Marti, 1967) is routinely applied (e.g., Strashnov and Gilmour, 2013; Leya et al., 2015). All stable and moderately long-lived Krypton isotopes (including ^{85}Kr, $t_{1/2} = 10.7$ yr, (Lerner, 1963)) are produced via spallation reactions (Gilabert et al., 2002) that are responsible for cosmogenic production. The main target elements for spallogenic Kr production are Rb, Sr, Y, Zr and Nb (Gilabert et al., 2002; Marti et al., 1966; Leya et al., 2015), which have isotopes similar in mass (slightly higher masses) to Kr isotopes. The minimum energies for neutrons producing Kr isotopes by spallation from Zr are 50 - 100 MeV (higher end of range for isotope masses < 83 (Gilabert et al., 2002)).

1.2 In situ produced terrestrial krypton

In meteorites, Rb, Sr, Y, Zr and Nb are trace constituents at the ppm level (Mason et al., 1976; Leya et al., 2004). A key conceptual step in utilizing in situ produced terrestrial krypton, Kr_{it}, is the realization that, due to the geochemical differentiation of the Earth, the target elements for cosmogenic Kr form discrete minerals, or are enriched in other minerals. For example: Rb is enriched in biotite; Sr forms strontianite ($SrCO_3$), strontian calcite (up to several % Sr) or coelestine ($SrSO_4$); Y forms xenotime (YPO_4); Zr zircon ($ZrSiO_4$) and baddeleyite (ZrO_2); and Nb is present in columbite (($Fe,Mn,Mg)Nb_2O_6$). Enrichments in these minerals over the concentrations in meteorites may be in the order of $10^3 - 10^4$, similar in magnitude to the cosmic ray flux differences between space and on Earth (Dunai, 2010), but in a reversed sense. The lower cosmic ray flux on Earth is thus fully compensated by the higher target-element concentrations and so determination of Kr_{it} in these minerals should be as easily attainable as Kr_{iet} is in meteorites.

Given the list of potential minerals, it appears that only zircon is near-ubiquitous on the Earth's surface, albeit as accessory mineral. Therefore, in the following we focus on zirconium as the target element and zircon as the target mineral. Considerations for other target elements/minerals are conceptually similar.

73 **1.2.1 Spallation**

74 As a first approximation of terrestrial production of krypton by spallation of zirconium due to neutrons

75 we use thick target, 1600 MeV proton-irradiation experiments (Gilabert et al., 2002), and derive ^{83}Kr as

76 the most abundant Kr$_{it}$-isotope, followed by ^{82}Kr, ^{81}Kr, ^{80}Kr, ^{78}Kr, ^{84}Kr, ^{85}Kr and ^{86}Kr (1 : 0.81 : 0.67 :

77 0.58 : 0.29 : 0.22 : 0.005 : 0.004; for shielding depth $\geq$ 49.2 g/cm^2; Fig. 1).
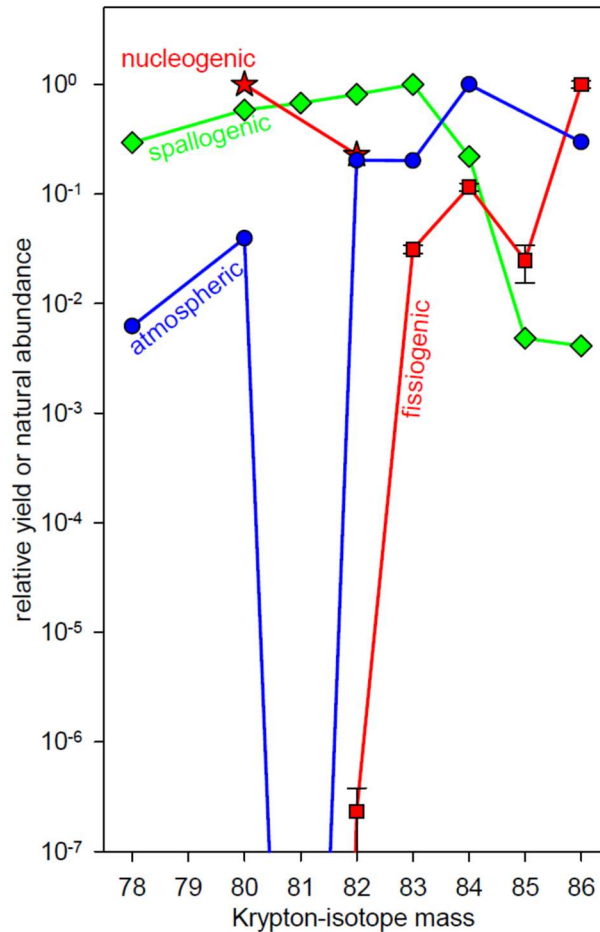
78

79 *Figure 1. Relative abundances of krypton isotopes in natural sources of krypton. Normalized krypton*

80 *abundances (normalized to the most abundant isotope of a given source) of atmospheric (Aregbe et al., 1996;*

81 *Sturchio et al., 2004), fissiogenic (from spontaneous fission of ^{238}U;(Jaea)), nucleogenic (thermal neutron*

82 *capture by bromine; (Soppera et al., 2014; Kendrick, 2012)), and spallogenic (proton irradiation experiments,*

83 *zirconium, $\geq$49 g cm-2 shielding; Table 2a of Gilabert et al., 2002) krypton. Most geological material on Earth*

84 *contains atmospheric krypton, with all large geochemical reservoirs (i.e., mantle, crust) containing krypton of*

85 *atmospheric composition.*

86

87 The dominant reaction pathway for spallogenic Kr production on zircon appears to be of the type

88 Zr(n,2α + xn)Kr (with neutron multiplicities x = 0, 1, 2, 3, 4, 5). This may be deduced from (i) the

89 minimum energies required and (ii) the Zr- and spallogenic Kr isotope abundances (Gilabert et al.,

90 2002). At the low energy end (50 MeV (Gilabert et al., 2002)) only α-emissions are possible. This is due

91 to the energy bonus of the emission of α-particles as compared the emission of individual nucleons,

which is 28.3 MeV per α-particle (Dunai, 2010), the binding energies of nucleons (neutrons and protons) are 8.7 MeV in this mass range (Soppera et al., 2014), protons additionally requiring >8 to overcome the Coulomb barrier. Consequently, individual separation of two neutrons and two protons from a nucleon in this mass rages would require an energy input from a cosmic ray particle of ≥50.8 MeV, whereas the separation of an α particle requires only ≥22.5 MeV. The most abundant spallogenic Kr isotope ^{83}Kr may be produced on the lightest and most abundant stable Zr-isotope ^{90}Zr (51.45%) via the energetically favourable (n, 2α) reaction (Fig. 2), however, also on all other Zr-isotopes via (n, 2α + xn) reactions (x = 1,2,4,5). Kr isotopes with masses smaller than 83 require in any case the additional separation of one or more neutrons, meaning higher minimum energies of the incoming neutrons are needed (Gilabert et al., 2002), which in turn explains the successively lower production as masses decrease. The lower production of ^{84}Kr is commensurate with the lower cumulative abundance of its target nuclides ^{91,92,94}Zr and, in the case of ^{92}Zr and ^{94}Zr, the requirement for the additional separation of one or two neutrons, respectively. The conspicuous relative rarity of spallogenic ^{86}Kr (Fig. 1), despite it being the Kr isotope closest in mass to Zr, probably stems from the fact that there is no (n, 2α + xn) pathway to produce it on stable Zr isotopes (Fig. 2).

Figure 2. Excerpt of the nuclide chart of the region relevant for spallogenic and muogenic production of cosmogenic Krypton from its main target elements (Rb, Sr, Y and Zr; Gilabert et al., 2002; Marti, 1967). Stable isotopes (and isotopes with half-lives > Gyr; white) are shown with their natural abundance (in %; Soppera et al., 2014). The long-lived nuclides ^{81}Kr and ^{85}Kr nuclides (i.e., half-lives > 1 yr, grey) are shown with their half-lives (Soppera et al., 2014). Nuclides to the left of the field of stable nuclides (yellow) decay via β$^+$ (positron) emission or electron capture, nuclides to the right of the stable nuclides (green) decay via β$^-$ (electron) emission from their nuclei. For illustration for how to 'read' the chart for nuclear reactions, examples for reactions producing ^{82}Kr from ^{90}Zr are shown at the bottom of the figure.

1.2.2 Negative muon capture

Muons (μ$^-$, μ$^+$), which are products from cosmic ray interactions in the Earth's atmosphere (Dunai, 2010; Stone et al., 1998) may also contribute to Kr production. Captured negative muons neutralize one proton and deliver 106 MeV (the mass of a muon at rest) to the nucleus (Dunai, 2010; Stone et al., 1998). Much of this energy is carried away by neutrino emission (ν_μ), such that on average close to 20 MeV are available for nuclear evaporation (Measday, 2001; Lifshitz and Singer, 1980). In the mass range of Zr-isotopes, captured negative neutrons may induce (μ$^-$, ν_μ + α) reactions with probabilities close to 10^{-4} (Wyttenbach et al., 1978). Production of krypton by muon capture on zirconium would require the separation of one additional charged particle, following reactions of the type (μ$^-$, ν_μ + 2αxn) and (μ$^-$, ν_μ + αpxn), with x = 0 to 4. The (μ$^-$, ν_μ + 2αxn) reaction would produce a radioactive Br-isotope decaying into a Kr isotope (Fig. 2). This would work for Kr isotopes with mass ≤ 84, except for ^{81}Kr as it is

4

129 shielded by stable [81]Br. Using the Coulomb barrier and reaction probability observed by Wyttenbach et

130 al. (1978), we estimate that probabilities for (μ^-, ν_μ + αp) and (μ^-, ν_μ + 2α) reactions are at least 10^2 to 10^3

131 lower than a (μ^-, ν_μ + α) reaction for a given Zr-isotope. The required separation energy for emission of

132 one or more neutrons (~ 8.7 MeV per neutron, see above) would decrease the likelihood of this even

133 further (Lifshitz and Singer, 1980). Hence, the probability of negative muons captured by Zr-isotopes

134 producing Kr isotopes is smaller than 10^{-6}. Of muons coming to rest in zircon, 35 ± 4 % are captured by

135 Zr (Von Egidy and Hartmann, 1982) and so the Kr isotope yield from muon capture by Zr in zircon is

136 less than 0.3 ppm. This translates into less than 10^{-6} atoms g^{-1} yr^{-1} at sea level and high latitude (Stone et

137 al., 1998).

138

139 **1.2.3 Interfering components**

140 Geochemical components that may interfere with the analysis of cosmogenic krypton are the products of

141 spontaneous fission of ^{238}U (fissiogenic krypton, Kr_{fis}) and neutron capture by bromine (nucleogenic

142 krypton, Kr_{nuc}). These may become important when analysing U- or Br-rich minerals (Eikenberg et al.,

143 1993; Honda et al., 2004; Ruzie-Hamilton et al., 2016; Kendrick, 2012). Fission yields of krypton

144 isotopes heavier than ^{81}Kr increase with increasing mass such that $^{86}Kr_{fis}$ is the most abundant, and the

145 yield of $^{82}Kr_{fis}$ is negligible (Fig. 1; (Eikenberg et al., 1993; Jaea)). Spontaneous fission of ^{238}U does not

146 produce Kr isotopes lighter than ^{82}Kr. $^{80}Kr_{nuc}$ and $^{82}Kr_{nuc}$ may be produced by reactions on bromine,

147 $^{79}Br(n,\gamma)^{80}Kr$, $^{81}Br(n,\gamma)^{82}Kr$ (reaction cross sections for thermal neutrons are 10.32 and 2.36 barn,

148 respectively (Soppera et al., 2014)). Bromine concentrations are low in silicate minerals (Kendrick,

149 2012; Ruzie-Hamilton et al., 2016; Teiber et al., 2015) but commonly not well constrained. The major

150 geochemical reservoirs of Earth (e.g., mantle) contain krypton close to atmospheric composition (^{80}Kr

151 2.25%; ^{82}Kr 11.6%; ^{83}Kr 11.5%; ^{84}Kr 57.0%; ^{86}Kr 17.3%; ^{78}Kr 0.35%; ^{81}Kr 0.5 ppt; (Buizert et al., 2014;

152 Aregbe et al., 1996)). Natural krypton is rarely measured in geological material due to the anticipated

153 consistency of these values (Broadley et al., 2020; Trieloff et al., 2000).

154

155 **1.2.4 Test of feasibility**

156 To test the feasibility of using Kr_{it} for Earth surface science applications, we analysed a suite of zircon

157 samples from near-surface sediment and bedrock with a wide range of anticipated exposure histories.

158 The sediment samples are zircon megacrysts from kimberlitic, carbonatitic and metamorphic source

159 rocks from locations in Australia (Mud Tank carbonatite; (Crohn and Moore, 1984; Currie et al., 1992)),

160 Tanzania (Singida kimberlite field and Ubendian-Usagaran metamorphic belt (Mannard, 1962; Kabete et

161 al., 2012)) and Germany (Ebersbrunn diatreme, Vogtland (Schmidt et al., 2013; Modalek et al., 2009)).

162 The bedrock samples are from glacially scoured surfaces and a block from the Grimsel Pass,

163 Switzerland (Wirsig et al., 2016). We use this suite of samples (see section 2 for details) to constrain

164 terrestrial production ratios of Kr_{it}-isotopes, to cross-calibrate production rates with a well-established

165   cosmogenic nuclide (^{10}Be), and to provide the first applications by constraining histories of burial and

166   exposure in arid and temperate regions.

167

168   **2. Sample materials**

169   **MUD:** These zircons are from the Mud Tank carbonatite, Northern Territories, Australia (23°0'47"S;

170   134°16'45"E, 660 m) (32, 33, 83)(Crohn and Moore, 1984; Currie et al., 1992; Gain et al., 2019;

171   Woodhead and Hergt, 2005). The carbonatite has a crystallization age of 731.0 ± 0.2 Myr (Gain et al.,

172   2019), protracted cooling or a later thermal overprint during the Alice Springs Orogeny (450–300 Myr)

173   is indicated by Pb-loss from some zircons (Gain et al., 2019). The emplacement occurred at

174   temperatures ≤ 650 ºC, in a fluorine rich environment (Currie et al., 1992). Zircons from this location

175   have a median Hf-concentration of 1.18 % (1st quartile 0.91%, 3nd quartile 1.19% (Woodhead and

176   Hergt, 2005)). The two carbonatite bodies that constitute this occurrence rise about 10 m above the

177   surrounding low-gradient landscape (Australian_Vermiculite_Industries, 2013). The elevation of

178   possible sampling locations is 660 ± 5 m.

179   The material used in this study was obtained commercially via a private vendor, as part of two 1 kg

180   batches of zircon sourced from an estate. The zircons were collected in the 1980s, when zircons were

181   still abundant at the surface, prior to the Mud Tank becoming a well-frequented mineral collection site

182   ('fossicking area'; (Australian_Vermiculite_Industries, 2013)). The zircons are sub-rounded, some show

183   percussion marks from fluvial transport and fractured surfaces show signs of subsequent abrasion (Fig.

184   3). Most have a lighter colour than excavated zircons from the same site (the latter purchased from

185   Dehne McLauchlin, Tasmania, Australia), suggesting bleaching from extended periods of exposure to

186   sunlight (Gain et al., 2019). We assume that the zircons analysed were predominantly sampled from the

187   surface. Individual zircons were crushed using a diamond mortar and subsequently sieved.

188   **SING:** These samples are from the Singida kimberlite field, Tansania (Mannard, 1962). The samples

189   were obtained commercially (Mawingu Gems, Idar Oberstein, Germany). At least 54 diatremes

190   (Mannard, 1962) occur in an area of about 1900 km^2 centred around 4°57'S, 34°25'E. The zircon-bearing

191   kimberlites intruded into the Cretaceous African surface (Mannard, 1962; King, 1978) during the

192   Eocene (Harrison et al., 2001) at an altitude ranging from 1100 to 1500 m (Harrison et al., 2001). We

193   adopt an elevation of 1300 m for scaling, when comparing the results from Singida with other locations.

194   The U-Pb ages of all (n=9) but one of the zircons used in this study are, within their individual

195   uncertainties, identical to their mean age of 44.8 ± 0.2 Myr (±1SD; Table 2). One sample (SING-21)

196   gives an age of 40.5±0.8 Myr (±1SD; Table 2). Remnants of the original tuff-rings are sometimes

197   preserved (Harrison et al., 2001; Mannard, 1962) so the long-term erosion rates are presumably low.

198   Much of the area is capped by relict calcretes and silcretes (Mannard, 1962). The area is covered by dry,

199   deciduous woodland, currently receiving 520 ± 260 mm annual rainfall (Harrison et al., 2001; Mannard,

1962). Zircons are concentrated in river sands near the pipes (Mannard, 1962), where they are mined in small pits down to several metres depth. We assume such a source for our samples.

The individual 5 to 10 mm sized crystals (Fig. 3) are of gem quality. Their outsides show surface roughing and small percussion marks from fluvial transport. Their Hf-concentrations range between 0.6 and 1.1% (Table 2). Individual zircons were crushed using a diamond mortar and subsequently sieved.

RBM, GOEL & VOGT: These zircons stem from a kimberlitic diatreme near Ebersbrunn, Vogtland, Germany (Schmidt et al., 2013; Modalek et al., 2009). Ages of zircons from this location were determined as 71.1±0.8 Myr (U-Pb; Table 2), which we take as the intrusion age. The diatreme is located on a topographic saddle (450 m elevation) in a soil-mantled landscape of moderate relief. The diatreme was first inferred through geophysical surveys and subsequently confirmed via shallow drill cores (Schmidt et al., 2013).

Zircons were obtained from local collectors, either commercially from a private vendor (VOGT) or provided in exchange (RBM, GOEL; from Sven Kreher, Goldmuseum Buchwald, Germany). They were extracted from modern stream/river-bed sediments in the Göltzsch near Netschkau (VOGT; GOEL: 300 m, 50°37'25"N, 12°14'47"E), and its tributary Raumbach (RBM: 380 m, 50°37'0"N, 12°21'24"E). The headwaters of the latter originate in the diatreme. The sampling site for RBM zircons is ~ 5 km downstream of the diatreme, those of VOGT and GOEL ~15 km. The smaller zircons (5-10 mm; all RBM and GOEL 1, 2 & 3) are mostly transparent, the pebble-sized zircons are opaque to translucent (all VOGT and GOEL 4 & 5; Fig. 3). Individual zircons were crushed using a diamond mortar and subsequently sieved.

SUM: These zircons are from the area around Sumbawanga, Tanzania (1850 m, 7°58'S, 31°37'E). The samples were obtained commercially (Mawingu Gems, Idar Oberstein, Germany). Potential source rocks are Paleoproterozoic metamorphic rocks (Kabete et al., 2012). We adopt an elevation of 1850 m for scaling but the actual elevation of the source and/or finding location may be higher. The samples exhibit signs of fluvial transport such as edge-rounding and percussion marks (Fig. 3). We assume that these samples were retrieved from stream sediments or sedimentary deposits. The samples are from two different batches (SUM 18 A & B; the other SUM 15 & 16) and possibly stem from different locations. Individual zircons were crushed using a diamond mortar and subsequently sieved.

GRIM: These samples (GRIM 19-1; GRIM 19-2; GRIM -1) are from Nägelisgrätli, east of Grimsel Pass, Switzerland. The Nägelisgrätli is part of the transfluence pass through which the last-glacial maximum Aare glacier was fed from the Rhône ice dome (Wirsig et al., 2016). [10]Be concentrations in quartz-samples from the Nägelisgrätli are consistent with a single stage exposure history, with complete resetting of signals of prior exposure via glacial erosion (Wirsig et al., 2016). The Grimsel Granodiorite (part of the Central Aar Granite) has an intrusion age of 298±2Ma (Schaltegger and Corfu, 1992) and was subsequently affected by regional metamorphism during the Alpine orogenesis around 30–35 Myr ago (Hettmann et al., 2009).

236   Samples for the current study were taken at 2390 m (GRIM 19-1: 46°33'57.66"N, 8°20'46.57"E; GRIM

237   19-2: 46°33'57.58"N, 8°20'46.71"E) and 2478 m (GRIM-1: 46°34'13.9"N, 8°21'6.4"E) elevation.

238   GRIM-1 and GRIM 19-1 are bedrock samples (Fig. 4). GRIM 19-2 a loose block in a shallow

239   depression (Fig. 4) and was presumably ice-transported to this location, as all other means of transport,

240   such as falling or rolling from uphill, can be excluded. The topography in the immediate vicinity of the

241   sampling sites is favourable for accumulating significant snow cover (significant in terms of capability

242   to reduce cosmogenic nuclide production). We performed no snow-cover corrections, since the main

243   purpose of these samples is to cross-calibrate production rates of cosmogenic nuclides that are equally

244   affected by snow-cover, i.e., snow-cover effects cancel each other out. The same applies to topographic

245   shielding corrections, which we likewise did not apply. Electro pulse disaggregation of samples and

246   subsequent zircon separation, by standard magnetic and heavy liquid techniques, was conducted by

247   Zirchron LLC, Tucson, Arizona, USA. The zircon grains are < 125 microns (Fig. 3).

248
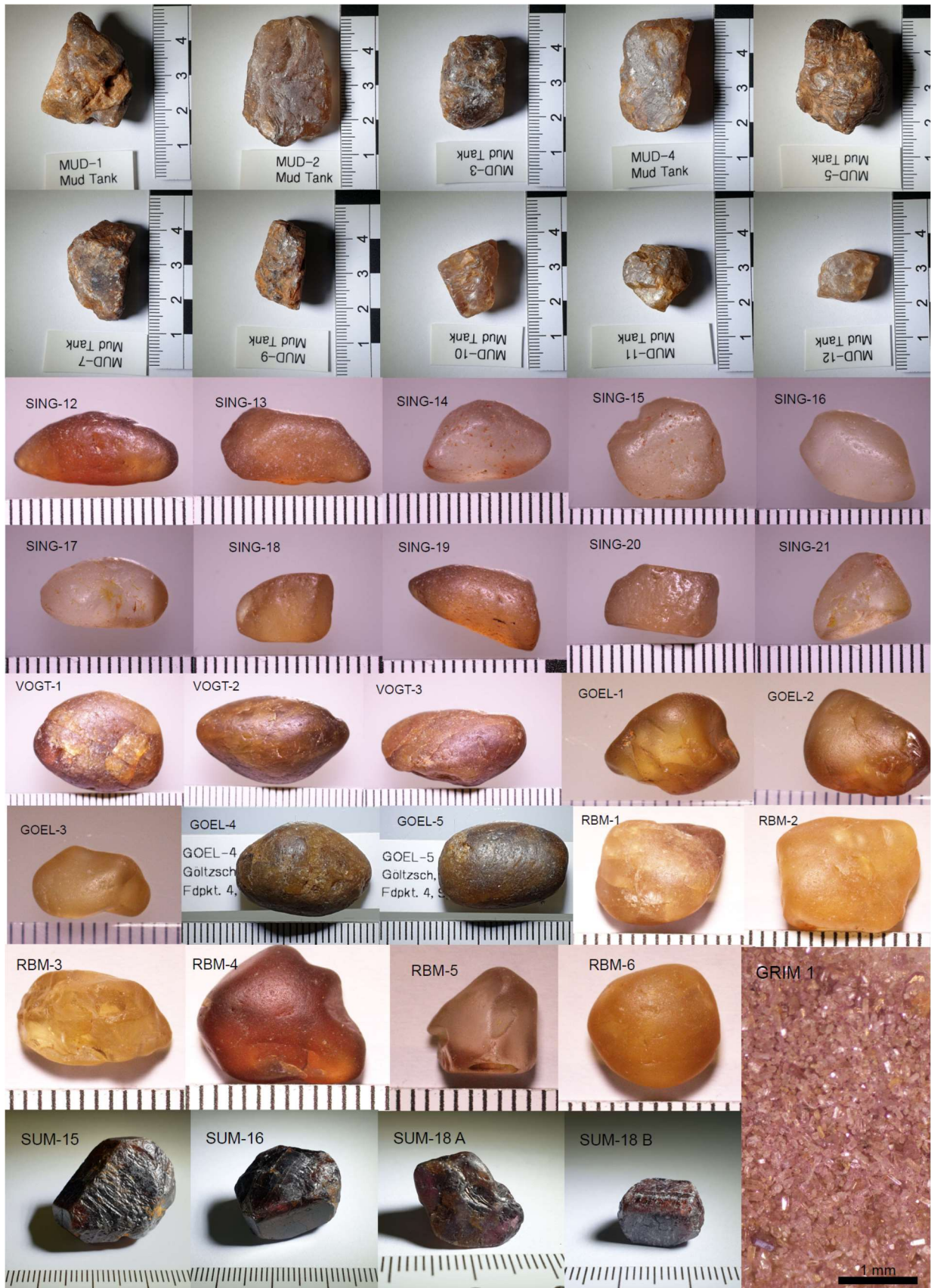
Figure 3: Photos of the zircons investigated. Scales are mm and cm. GRIM-1 is exemplary also for samples GRIM 19-1 and GRIM 19-2 (not shown). Crystals' weights are provided in Table 1 (where applicable).

253
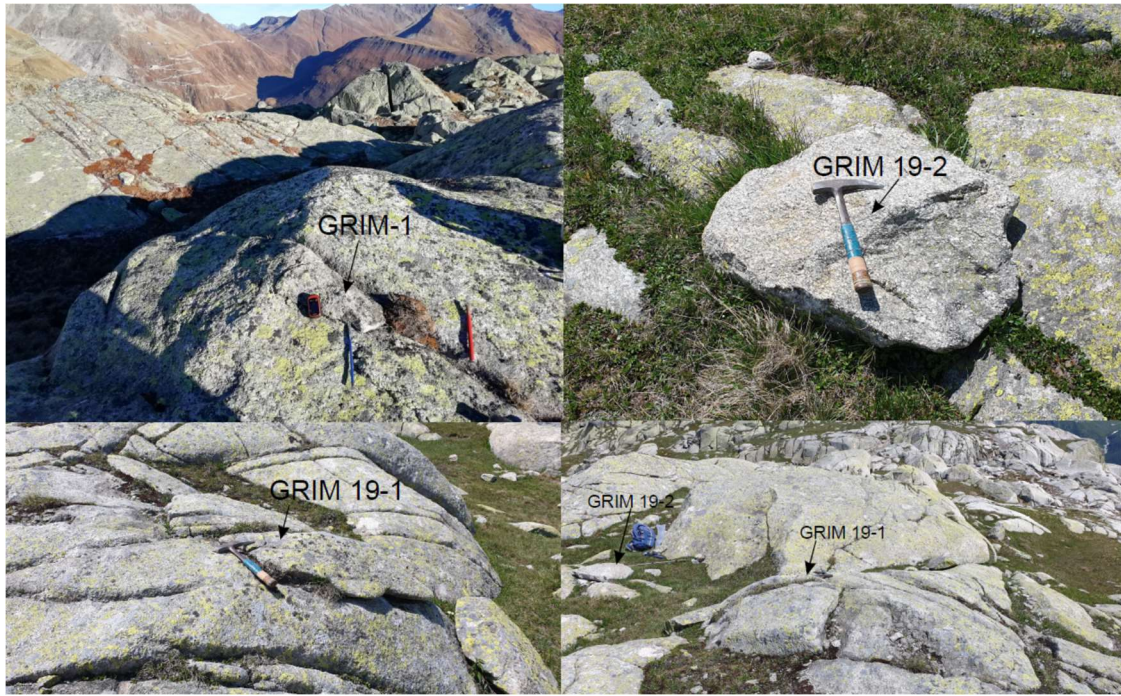
Figure 4: Samples and sampling locations on the Näglisgrätli, Grimsel Pass, Switzerland. Photo of GRIM 1 by
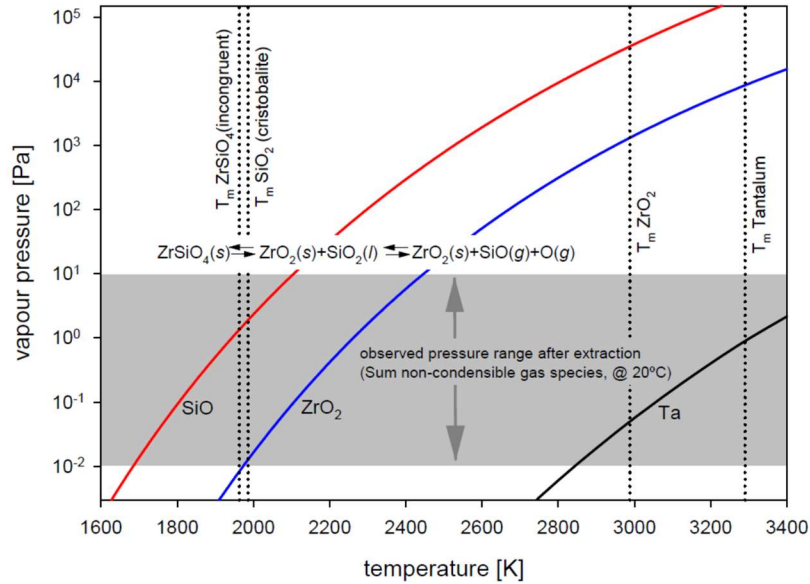*P. Abbott/ G. King; all others T. Dunai.*

3 Methods

3.1 Krypton isotope determinations

The general layout of the noble gas set-up at Cologne is described in Ritter et al. (2021), who focus on the analysis of cosmogenic neon. Here we reproduce some aspects of this description (Ritter et al., 2021), adding details that are pertinent for Kr extraction from zircon and cosmogenic Kr analysis.

### 3.1.1 Krypton extraction from zircon

Samples are placed into tantalum tubes (4 mm outer diameter, ca. 12 mm long) that are pinched off at both ends. The tantalum tubes are placed into tungsten cups, which in turn are placed into a molybdenum sample revolver. For thermal insulation, several fragments (250-500 micron) of zirconia (cubic stabilized zirconium oxide, melting point ~2700°C) are placed between the cups and revolver. Energy for the heat-extraction in vacuum is provided by an output-tuneable 600 W fiberlaser (Rofin StarFiber600) at 1064nm wavelength through galvanometer scanner optics (Rofin RS S 14 163/67 0°), a UV-grade fused silica viewport (MDC Precision, 9722005) and a single-use fused-silica protective glass (Thorlabs, WG41050). The tantalum-tubes are heated via scanning a continuous wave beam with 200W power for a total of five minutes. The scanning speed is 20 cm/s; first rastering a rectangular area of 4 by 10 mm with a defocussed beam (~ 0.5 mm diameter) for three minutes, then with focussed beam a circular area with 5 mm diameter, on the then shrivelled tube, for two minutes. The temperature achieved is sufficient to melt the top of the Tantalum tube (melting point of Tantalum is 3020 ± 15 °C; (Arblaster, 2018)) and to quantitatively sublimate the silica content of zircon. Zircon melts

incongruently above ~1690°C (Kaiser et al., 2008) and the silica is presumably lost as silicon monoxide and oxygen (Fig. 5; Schick, 1960). Silicon monoxide is observed as brown coating on the protection windows; the coating starts to appear within about one minute after starting the laser extraction. The quantitative loss of silica is verified by weighing of the tantalum tubes after heat-extraction; in most cases, the measured loss indicates also partial sublimation of ZrO_2 (Fig. 6; Hoch et al., 1954).

Figure 5: Vapour pressure of Silicon monoxide (SiO), zirconia (ZrO_2) and tantalum (Ta) as a function of temperature (Schick, 1960; Hoch et al., 1954; Arblaster, 2018; Kaiser et al., 2008), and the melting points of zircon ($ZrSiO_4$), cristobalite (SiO_2) and zirconia (Kaiser et al., 2008). Zircon melts incongruently to ZrO_2 and SiO_2-melt (the melting temperature of the high-temperature modification of SiO_2, cristobalite, is only ~10K higher than that of zircon) (Kaiser et al., 2008). At a given temperature the vapour pressure of SiO is one to two orders of magnitude higher than that of ZrO_2, the larger differences are at lower temperatures. Above the melting point of cristobalite, SiO can boil off, rather than sublimate from the surface of a solid (as is the case for ZrO_2, below its melting point), if the pressure in the extraction cell is lower than the vapour pressure. Observations of the residual pressure of non-condensible gases after extraction (at this time the laser furnace is still hot from the extraction, but the laser power is switched off) indicate that in our experimental setup SiO may boil off at temperatures > 2100K. The higher vapour pressure and the ability to boil off from a liquid lead to a preferential loss of SiO, as compared to ZrO_2, from zircon at high temperatures.
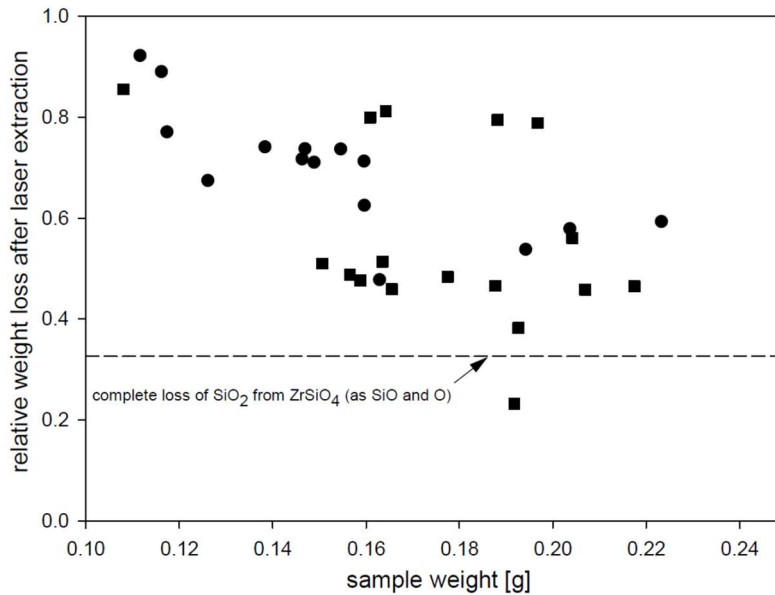
Figure 6: Relative mass loss of zircon samples after laser extraction as a function of initial sample weight. Squares denote samples with grain sizes above 125 μm, circles denote samples that (also) contain grains smaller 125 μm. All but one sample (RBM-6) have completely lost their constituent SiO₂ and some of the ZrO₂ residue (see also Fig. 5).

3.1.2 Krypton isotope determination

Subsequent to the extraction, the evolved gases cleaned by sequential exposure to two reactive metal getters (SAES NP50) and a stainless steel watertrap (held at 205 K). The noble gases are separated cryogenically on a stainless steel coldtrap (Janis, twin coldhead model 204): neon and heavier noble gases are quantitively condensed on the trap at 24 K; the trap is then heated to 120 K and pumped (neon and argon are removed; >99% of Kr remains on the trap); finally, the trap is heated to 240 K to release Kr for analysis in a noble gas mass spectrometer.

The noble gas mass spectrometer (Helix MCPlus, Thermo Fisher Scientific) is equipped with five Combined Faraday Multiplier modules (CFM). One CFM is fixed in axial position (Ax) and two movable CFM are each on the low (L1, L2) and the high (H1, H2) mass side of Ax. The L1 CFM is flipped as compared to the factory-standard configuration (lateral positions of multiplier and faraday slits are swapped). Four Faraday collectors are fitted with 10^{13} Ω pre-amplification resistors (H1, Ax, L1, L2), one with 10^{12} Ω (H2). The multipliers are operated in ion-counting mode. One CFM module (L1 position) has a higher resolution (0.3 mm entry slit), the others have regular resolution (0.6 mm slits). At the operation conditions we used for krypton analysis (source slit 0.25 mm; 10 KV acceleration voltage), mass resolution (at 5% peak valley) and mass resolving power (between 10% and 90% of peak) on the L1 detector with 0.3 mm collector slit width are ~1700 and ~6500, respectively. For the detectors with 0.6 mm collector slit, the corresponding values are ~1000 and ~6000, respectively. This resolution allows the full separation of krypton isotopes from hydrocarbon isobars (~600 is required; Burnard et al., 2013). The resolution of the L1 detector achieves separation of $^{40}Ar_2H^+$ from $^{81}Kr+$ at

323    $^{81}Kr^+$-peak centre. Partial resolution is achieved on the remaining detectors, permitting interference-free

324   ($^{40}Ar_2H^+$) analysis of $^{81}Kr^+$ in an off-centre position. Interference of $^{80}KrH^+$ on $^{81}Kr^+$ cannot be resolved;

325   we determine the $^{84}KrH^+/^{84}Kr^+$-ratio during calibration gas measurements (observed range 2 - 5 x 10^{-6};

326   n=26) as a proxy for the $^{80}KrH^+/^{80}Kr^+$-ratio and correct sample signals accordingly. Likewise, the

327   interference from $^{81}Br^+$ cannot be resolved, we corrected it via monitoring and subtracting the

328   background at the position of $^{81}Kr^+$ during blank measurements. This background was found to be stable

329   at the equivalent of 2200 ± 200 (n=7; 1SD) atoms ^{81}Kr. Using multiples (m) of the blank value (2200 ±

330   200 atoms), we estimate the detection limit for ^{81}Kr with the current setup is ~ 7000 atoms (m=3).

331   Blanks yield 0.65±0.30 attomol ^{84}Kr (n=8). Measurements of hot blanks 0.75±0.25 attomol ^{84}Kr (hot

332   laser extraction, n=5, 1SD of mean), cold blanks 0.55±0.05 attomol ^{84}Kr (same volume, but laser power

333   off, n=2, 1SD of mean), or the line blank 0.5±0.1 attomol ^{84}Kr (purification line only, without the laser

334   extraction volume, n=1, 1SD of measurement) are indistinguishable from each other. The observed Kr

335   blanks are about four-times lower than the lowest reported previously (Zimmermann et al., 2018).

336

337   We analysed the krypton isotopic abundances in multicollection mode. First, masses 78 to 85 are

338   measured in four cycles on the multipliers; 1st: $^{84}Kr(H2)$, $^{83}Kr(H1)$, $^{81}Kr(Ax)$, $^{80}Kr(L1)$, $^{78}Kr(L2)$; 2nd:

339    $^{83}Kr(H2)$, $^{82}Kr(H1)$; 3rd: $^{82}Kr(Ax)$, $^{81}Kr(L1)$; 4th: $^{84}KrH^+(H2)$, $^{84}Kr(H1)$, followed by sequential analysis

340   of masses 86, 84, 83 and 82 on the axial Faraday cup. Gain calibrations of multipliers are performed

341   relative to the H1 multiplier, using the measurements of calibration gas (air-pipette, containing

342   11.25±0.01 fmol Kr) and the isotopic composition of air (Aregbe et al., 1996). The gain of the H1

343   multiplier is in turn calibrated to the axial Faraday collector using the corresponding $^{84}Kr^+$ readings of

344   calibration gas measurements. Within each of the two measurement periods, the variability of ^{84}Kr

345   Faraday signals for calibration gas were smaller than ± 1% (1 SD, n=26). Between the two periods the

346   ion source was switched off and after turning the source back on the sensitivity had dropped by 4%.

347   Calibration gas was measured prior to a set of two or three sample measurements on a given day, with

348   these preceding calibrations used for gain calibration and interference correction ($^{80}KrH^+$) of the

349   subsequent samples. We use both determinations of ^{81}Kr, on Ax (off-centre) and on L1, to obtain an

350   error weighted mean of intensities. We calculate the concentration of $^{78}Kr_{it}$ from the measured $^{78}Kr/^{82}Kr$

351   ratio, assuming that all ^{82}Kr is atmospheric. The $^{81}Kr_{it}$ concentration is corrected for interferences ($^{81}Br^+$,

352    $^{80}KrH^+$).

353

354   **3.2 ^{10}Be determination**

355   Samples were ground and sieved to 250-1000 μm and subsequently purified through sequential HF-

356   leaching (Kohl and Nishiizumi, 1992). ICP-OES was used to verify the purity of the quartz before

357   dissolution. ^{10}Be AMS (Accelerator Mass Spectrometry) targets were prepared using the stacked column

358   approach (Binnie et al., 2015). A reagent blank and in-house quartz reference material (CoQtz-N;

359 (Binnie et al., 2019)) was prepared in tandem with the samples. AMS measurements were made on

360 CologneAMS (Dewald et al., 2013), normalized to the ICN standard dilutions prepared by Nishiizumi

361 for [10]Be (Nishiizumi et al., 2007). Concentrations of [10]Be are reported following blank subtractions,

362 which were less than 1% of the total number of nuclides measured. The 1 standard deviation analytical

363 precision of the nuclide concentrations was estimated by summing in quadrature the relative

364 uncertainties on the AMS measurements, both the samples and the blank, along with a 1% (1 SD)

365 estimate for the precision of the mass of [9]Be added during spiking. Concentrations obtained from

366 intercomparison material (CoQtz-N; (Binnie et al., 2019)) measured alongside the samples are

367 consistent with the long-term arithmetic mean $2.43 \pm 0.11 \times 10^6$ atoms g^{-1} CoQtz (1SD; N = 55) at our

368 laboratory.

369

370 **3.3 U-Pb-age determination**

371 U, Th and Pb isotopes of zircon were performed by LA-ICPMS at FIERCE (Frankfurt Element and

372 Isotope Research Center), Goethe University Frankfurt following the methods described in Gerdes et al.

373 (2009). A Thermo Scientific Element XR sector field ICP-MS was coupled to a RESOlution 193 nm

374 ArF Excimer laser (Compex Pro 102, Coherent) equipped with an S-155 two-volume ablation cell

375 (Laurin Technic, Australia). The GJ-1 zircon (603 ± 1 Myr) was used as primary zircon reference

376 material (RM) and RMs BB-16, Plešovice and Monastery zircon for validation of the analytical results.

377 The results obtained on these zircon RMs were within 0.8% or better of the reported ages. Data

378 processing (including common lead correction) was performed using an Isoplot (Ludwig, 2012)-

379 supported Microsoft Excel-based spreadsheet (Gerdes and Zeh, 2009). Uncertainties reported are at the

380 2SD level (i.e. 95% confidence) and are calculated by quadratic addition of the internal uncertainties

381 (SE), counting statistics, gas-background uncertainties, common Pb corrections, the excess of scatter

382 derived from the primary RM.

383

384 **4 Results**

385 The results of the, Krisotope determinations, U-Pb age-determinations, and the [10]Be-results are provided

386 in Tables 1, 2 and 3, respectively.

387

SampleD	weight crystal [g]	grain size§ [µm]	weight analysed [mg]	^{84}Kr/^{82}Kr	^{83}Kr/^{82}Kr	^{80}Kr/^{82}Kr	^{78}Kr/^{82}Kr	^{82}Kr [10^8 g^{-1}]	^{81}Kr [10^6 g^{-1}]	^{78}Kr$_{cos}$ [10^6 g^{-1}]
SING-12	1.42	75-250	162.9	4.475(19)	0.9855(39)	0.2124(10)	0.04087(28)	5.89(7)	1.03(3)	6.04(18)
SING-13	1.40	75-250	133.8	4.269(15)	0.9974(28)	0.2315(11)	0.04997(45)	6.41(8)	3.62(6)	12.4(3)
SING 14	1.21	75-250	116.2	4.496(13)	0.9825(22)	0.2400(12)	0.04126(41)	8.58(11)	2.69(6)	9.13(37)
SING-15	1.44	75-250	138.4	4.051(18)	0.9942(40)	0.2348(12)	0.05607(37)	5.04(5)	2.83(4)	12.8(2)
SING-16	1.19	75-250	111.6	3.952(14)	0.9733(26)	0.2373(13)	0.05640(42)	6.00(7)	0.626(41)	15.5(3)
SING-17	1.31	75-250	146.3	4.357(21)	0.9813(41)	0.2117(11)	0.04326(35)	5.35(5)	2.12(4)	6.75(2)
SING-18	0.91	75-250	126.2	4.415(24)	0.9767(50)	0.2113(14)	0.04079(45)	4.18(7)	0.152(30)	4.26(2)
SING-19	1.37	75-250	159.7	4.209(15)	0.9914(30)	0.2253(13)	0.05046(45)	3.75(5)	2.27(4)	7.44(2)
SING-20	1.35	75-250	159.6	4.335(22)	0.9830(49)	0.2166(13)	0.04470(53)	3.65(5)	0.154(26)	5.14(2)
SING-21	1.01	75-250	117.4	4.538(24)	0.9593(49)	0.1916(14)	0.03180(32)	6.33(8)	0.390(26)	0.75(2)
VOGT-1	7.75	125-250	199.8	3.903(27)	0.9826(65)	0.2377(19)	0.05671(48)	2.50(3)	0.267(19)	6.51(15)
VOGT-2	7.43	125-250	192.7	3.216(12)	1.0755(38)	0.3156(18)	0.09928(67)	2.78(5)	0.215(20)	19.1(4)
VOGT-3	4.49	125-250	156.5	3.561(13)	1.0688(32)	0.2964(14)	0.08662(53)	3.93(5)	0.271(22)	22.0(4)
GOEL-1	1.33	125-250	165.5	3.460(19)	1.0501(55)	0.2947(19)	0.08625(65)	3.85(6)	0.246(25)	21.4(4)
GOEL-2	1.60	125-250	160.9	4.189(18)	1.0030(41)	0.2360(13)	0.05380(62)	3.84(5)	0.205(27)	8.90(26)
GOEL-3	0.62	125-250	108.0	4.317(36)	0.9880(16)	0.2824(19)	0.04749(59)	9.54(14)	0.483(46)	16.1(6)
GOEL-4	8.11	125-250	214.5	4.047(17)	1.0178(40)	0.2437(12)	0.06067(58)	2.88(1)	0.270(21)	8.67(2)
GOEL-5	7.56	125-250	211.1	4.110(14)	1.0137(28)	0.2411(10)	0.05815(33)	4.38(6)	0.244(18)	12.0(2)
RBM-1	1.23	125-250	206.9	3.565(13)	1.0237(27)	0.2826(14)	0.08023(47)	4.57(6)	0.438(20)	22.7(4)
RBM-2	1.86	125-250	150.6	3.937(18)	1.0016(42)	0.2444(14)	0.06005(42)	4.22(4)	0.329(22)	12.4(2)
RBM-3	0.90	125-250	217.5	4.507(19)	0.9723(38)	0.2016(11)	0.03545(37)	2.77(3)	0.521(17)	1.34(1)
RBM-4	1.32	125-250	187.7	4.842(21)	1.0651(44)	0.2080(13)	0.05148(38)	3.49(5)	0.430(25)	7.29(17)
RBM-5	0.72	125-250	177.5	4.253(16)	1.0071(33)	0.2338(11)	0.05189(31)	5.56(8)	0.423(22)	11.8(2)
RBM-6	1.04	125-250	191.8	4.254(14)	1.0103(30)	0.2377(09)	0.05343(27)	8.20(9)	0.386(17)	18.7(3)
MUD-1	25.4	125-250	196.7	4.475(15)	0.9652(30)	0.2054(10)	0.03532(24)	2.87(4)	1.65(3)	1.35(7)
MUD-2	22.6	125-250	207.3	4.249(22)	0.9734(47)	0.2123(12)	0.04371(33)	3.12(3)	1.53(2)	4.09(11)
MUD-3	16.4	125-250	164.2	4.541(14)	0.9705(28)	0.2290(19)	0.03461(19)	3.64(5)	1.45(3)	1.45(7)
MUD-4	25.7	125-250	189.4	4.285(16)	0.9805(31)	0.2170(10)	0.04347(42)	3.36(4)	2.38(4)	4.32(15)
MUD-6	30.9	125-250	232.7	4.496(18)	0.9851(37)	0.2074(10)	0.03903(28)	3.47(4)	1.57(2)	2.92(1)
MUD-7	17.6	125-250	188.2	4.649(15)	0.9895(29)	0.2539(19)	0.03595(59)	4.85(6)	1.81(4)	2.58(29)
MUD-9	13.0	125-250	204.1	4.429(19)	0.9797(35)	0.2064(11)	0.03866(40)	3.36(4)	2.13(4)	2.70(14)
MUD-10	9.68	125-250	202.4	4.352(23)	0.9804(49)	0.2094(14)	0.04131(32)	3.22(3)	2.22(3)	3.44(11)
MUD-11	11.0	125-250	205.1	4.530(25)	0.9728(53)	0.1996(13)	0.03438(28)	2.66(3)	1.37(2)	1.00(7)
MUD-12	8.00	125-250	220.3	4.461(13)	0.9856(27)	0.2141(09)	0.04014(25)	4.50(6)	1.83(3)	4.28(13)
SUM-15	20.9	125-250	177.2	4.672(21)	1.0477(45)	0.2062(15)	0.03903(36)	2.75(4)	1.16(3)	2.31(10)
SUM-16	16.2	125-250	150.3	4.621(36)	1.0479(78)	0.2098(18)	0.04049(59)	2.96(4)	2.12(4)	2.93(18)
SUM-18A	3.08	125-250	158.8	4.612(19)	0.9816(37)	0.1933(10)	0.03242(47)	3.81(5)	1.48(4)	0.68(18)
SUM-18B	2.42	125-250	163.5	4.648(13)	0.9910(21)	0.2019(09)	0.03313(31)	4.87(5)	0.528(23)	1.22(15)
GRIM-1	n.a.	<125	223.3	5.110(28)	1.1300(57)	0.2025(14)	0.03159(38)	2.50(3)	0.482(20)	0.241(94)
GRIM-19-1A	n.a.	<125	203.7	5.097(28)	1.1121(59)	0.1985(12)	0.03158(25)	3.26(4)	0.445(19)	0.313(81)
GRIM-19-1B	n.a.	<125	194.2	5.011(26)	1.0860(52)	0.1975(13)	0.03109(37)	3.88(5)	0.480(19)	0.181(142)
GRIM-19-1C	n.a.	<125	148.9	5.091(12)	1.1084(23)	0.2033(07)	0.03177(31)	3.29(4)	0.462(27)	0.378(104)
GRIM-19-2A	n.a.	<125	154.6	5.053(23)	1.0996(46)	0.1975(12)	0.03135(30)	3.81(4)	0.424(26)	0.278(114)
GRIM-19-2B	n.a.	<125	146.9	5.080(20)	1.0980(42)	0.2019(11)	0.03141(20)	4.07(5)	0.415(26)	0.320(81)

388

389 *Table 1: The analytical uncertainties of the isotope ratios and abundances are 1SD, they are provided in*

390 *brackets as last significant digits. ^{78}Kr$_{cos}$ is calculated from the difference between the measured and the*

391 *atmospheric ^{78}Kr/^{82}Kr ratio (Aregbe et al. 1996). §grain size after crushing and sieving. GRIM-19-1A, -1B, and -*

392 *1C are aliquots of sample GRIM-19-1; GRIM-19-2A and -2B are aliquots of sample GRIM-19-2.*

Sample ID	U-Pb age [Myr]	Hf [ppm]
SING-12	45.14 ± 1.08	6980 ± 130 (n=6)
SING-13	45.14 ± 1.07	6870 ± 160 (n=7)
SING 14	44.86 ± 1.23	8760 ± 150 (n=7)
SING-15	44.86 ± 1.38	10200 ± 230 (n=6)
SING-16	44.83 ± 1.17	8010 ± 150 (n=6)
SING-17	44.36 ± 1.27	8650 ± 120 (n=6)
SING-18	44.70 ± 0.35	7870 ± 140 (n=6)
SING-19	44.80 ± 0.31	6410 ± 94 (n=6)
SING-20	44.51 ± 0.34	7960 ± 100 (n=6)
SING-21	40.47 ± 0.42	10810 ± 160 (n=7)
Göltzsch (zr1-4)	71.2±0.8	n.d.

Table 2: Laserablation ICP-MS age-determinations and Hf-concentrations of zircons from Singida, Tansania (samples 'SING'), and the Vogtland ('Göltsch (zr1-4)', mean age of four zircons from the same locality as samples 'VOGT' and 'GOEL'). The mean age of the samples from Singida is 44.80±0.24 Myr (1SD; n=9; SIN-21 excluded). Within their individual uncertainties, the individual ages of all zircons, bar SING-21, agree with this mean. The age of SING-21 is significantly (>3SD) lower than this mean. The numbers in brackets denote the number of analyses from which the mean Hf-concentration was calculated.

Sample	AMS ID	Lab ID	$^{10}Be/^9Be$	^{10}Be concentration [10^5 atoms/g]
GRIM-1	s16545	KL-1122B	$4.03 ± 0.13 \times 10^{-13}$	3.21 ± 0.11
GRIM-19-1	s16546	KL-1123B	$3.63 ± 0.12 \times 10^{-13}$	3.07 ± 0.11
GRIM-19-2a	s16547	KL-1124B	$3.03 ± 0.11 \times 10^{-13}$	2.44 ± 0.09
GRIM-19-2b	s16548	KL-1125B	$3.48 ± 0.12 \times 10^{-13}$	2.48 ± 0.09
chemistry blank	s16550	KL-B14B	$9.8 ± 3.3 \times 10^{-16}$	n.a.

Table 3: ^{10}Be results for quartz samples from the Grimsel Pass, Switzerland. GRIM-19-2a and GRIM-19-2b are duplicate measurements sample GRIM-19-2. The uncertainties denote the standard deviation (1SD). 10Be concentrations are reported after the chemistry blank correction. Samples, 24.03 to 28.33 g quartz, were spiked with 300µg Be using a commercial Beryllium ICP standard solution (Scharlau), with a concentration of 1000 mg/l traceable to NIST

4.1 Proof of concept for in situ produced terrestrial krypton

We find that all zircons analysed have $^{78}Kr/^{82}Kr$ and/or $^{80}Kr/^{82}Kr$ ratios that are distinct from air (Fig. 7). Most of the data fall on the air-cosmogenic mixing line with no apparent influence from mass fractionation or nucleogenic Kr (Fig. 7). Neither mass fractionation nor the addition of nucleogenic ^{80}Kr and/or ^{82}Kr can produce the main trend (Fig. 7). However, either process may account for samples deviating from the mixing line. Furthermore, all zircons contain quantifiable amounts of ^{81}Kr (Fig. 8) that, in the absence of alternative sources, must be cosmogenic. Both observations, the mixing array and the presence of ^{81}Kr demonstrate the feasibility of measuring Kr_{it} in terrestrial material.

Mass fractionation of noble gases is a common feature for samples originating from degassing magmatic systems (Kaneoka, 1980). Samples may contain residual gas from diffusive loss (enriched in heavy isotopes), or trapped gas that was fractionated during diffusion from minerals and/or degassing from melts (enriched in light isotopes). The resulting mass fractionation causes samples to plot along a path that deviates from the spallation line (Fig. 7). The samples that lie above the spallation line and to the left of the mass fractionation line (two from Mud Tank, one each from Singida and Vogtland) must contain some nucleogenic Kr; requiring bromine in the host rocks, their sources, and/or the samples themselves. Structurally there is no suitable site for bromine in the zircon lattice, so if present it is trapped in fluid or melt inclusions. Sources for kimberlites appear to be rich in halogens and in bromine (Kamenetsky et al., 2014; Burgess et al., 2009), which could explain the presence of nucleogenic Kr in some Singida and Vogtland zircons. The original melt, or source, of the Mud Tank carbonatite was rich in halogens (Currie et al., 1992), presumably containing sufficient bromine to give rise to significant nucleogenic Kr. Fractionation and the presence of nucleogenic Kr are interesting on their own account; to our knowledge natural nucleogenic Kr has not been reported before. However, for the purpose of the present study, we limit the use of the Krypton triple-isotope plot (Fig. 7) to discern samples with a simple Kr_{atm} and Kr_{it} mixture from those with complex components.

4.2 Production ratios of terrestrial cosmogenic krypton isotopes

In detail, the atmospheric - spallogenic mixing trend in $^{78}Kr/^{82}Kr$ $^{80}Kr/^{82}Kr$ space (Fig. 7) that is defined by our results is slightly steeper than the one inferred from the proton-irradiation experiments (Gilabert et al., 2002) (zircon data: 1.682±0.015 (1SD) vs. proton irradiation ≥ 49.2 g cm^{-2} shielding: 1.592±0.020 (1SD); Fig. 7). Hence, the $^{78}Kr/^{82}Kr$ and/or $^{80}Kr/^{82}Kr$ production ratios appear to be different by $\sim 4\%$ in the zircons as compared to the irradiation experiment. This small difference is unsurprising considering that in the proton irradiation experiments the 1600 MeV primary proton beam, as well as secondary protons and neutrons, produce Kr isotopes in roughly similar proportions (Gilabert et al., 2002), whereas near the Earth surface secondary neutrons dominate (~90% at sea level (Dunai, 2010)). We take the good agreement as indication that in the mass range of ^{78}Kr to ^{82}Kr the isotopic production ratios derived from proton-irradiation experiments (Gilabert et al., 2002) are a reasonable approximation for Kr produced by spallation on Zr near the Earth's surface.
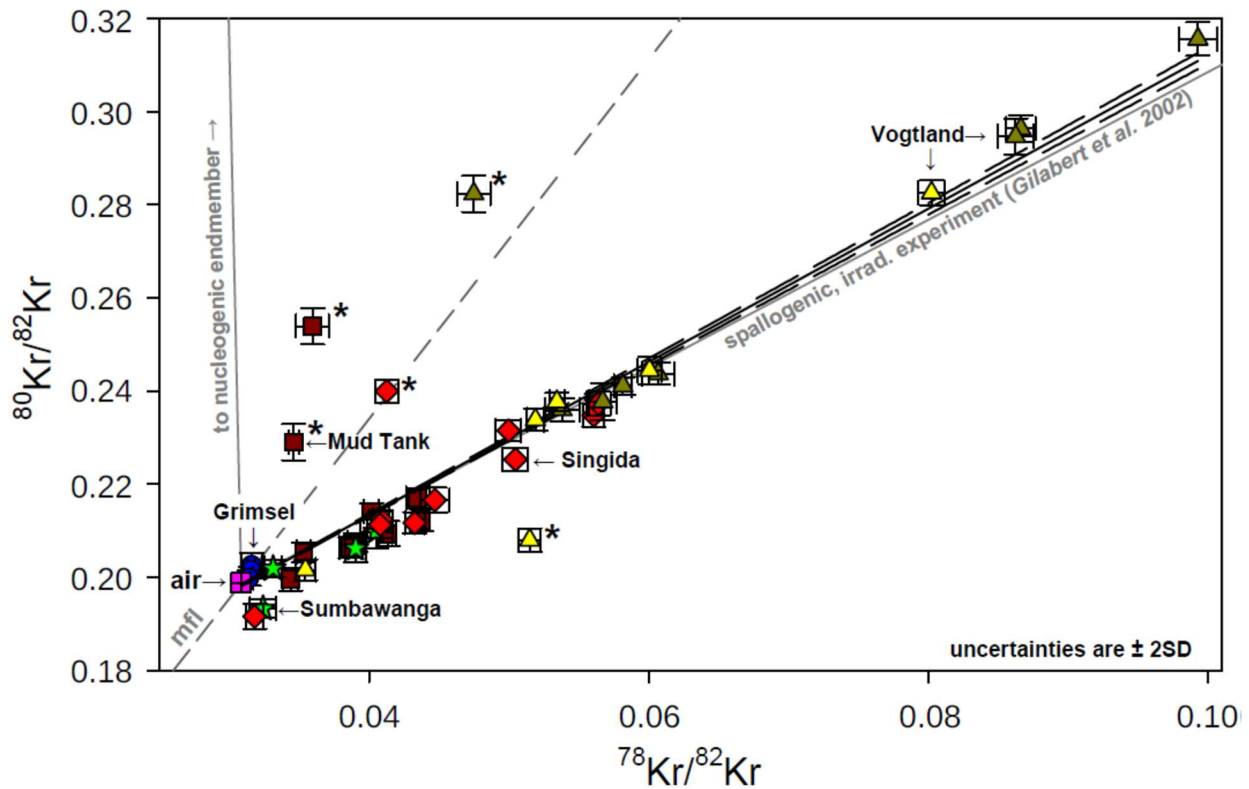
*Figure 7. Identification of krypton components and of processes fractionating krypton isotopes. Krdata from zircons of various locations, all of which have been exposed to cosmic rays at or near the Earth's surface, form a linear trend between air (atmospheric Kr; (Aregbe et al., 1996)) and a spallogenic endmember. Several samples plot far from this trend (marked with an asterisk *). They may contain fractionated Krypton ('mfl' mass-fractionation line; (Kaneoka, 1980)) and/or nucleogenic krypton. The linear least square regression of the data (performed with regression module of SigmaPlot 14) is shown by the solid black line and excludes measurements marked with an asterisk *. The regression is forced through air. The black dashed lines are the 95% confidence intervals of the regression line. Regression of the Kr concentrations from the zircon samples indicates that the terrestrial cosmogenic endmember is slightly different to that obtained from proton irradiation experiments (solid grey line; (Gilabert et al., 2002)). Brown squares are Mud Tank carbonatite; red diamonds are for the Singida kimberlite field; green stars are Sumbawanga; blue circles are the Grimsel pass region; triangles represent Vogtland (dark yellow: samples GOEL & VOGT; yellow: samples RBM).*

4.3 Cross-calibration of ^{81}Kr and ^{10}Be production rates

In samples of glacially eroded rocks from the Grimsel Pass (Switzerland) we determined concentrations of both ^{81}Kr$_{it}$ in zircon and ^{10}Be in quartz (Tables 1 & 3). The resulting ^{81}Kr$_{it}$(zrc)/^{10}Be(qtz) ratio is 1.545±0.045 (1SE, error weighted mean, n=3). Using a ^{10}Be production rate of 4.10±0.17 atoms g^{-1} yr^{-1} (1SE; at sea level and high latitude (SLHL) for Europe (Martin et al., 2017); LSD scaling (Lifton et al., 2014), atmospheric pressure (Uppala et al., 2005)), we derive a SLHL ^{81}Kr$_{it}$ production rate of 6.33±0.32 atoms g^{-1} yr^{-1} (1SD) in zircon.

18

4.4 Histories of exposure and burial

Due to decay of ^{81}Kr, intermittent burial of samples lowers the measured ^{81}Kr/^{78}Kr$_{it}$ ratio with respect to the production ratio; with increasing exposure time at the surface, the measured ^{81}Kr/^{78}Kr$_{it}$ -ratio decreases as ^{81}Kr tends towards saturation concentrations. Hence, samples with the highest ^{81}Kr/^{78}Kr$_{it}$ - ratio for a given ^{81}Kr concentration (^{81}Kr concentration is a proxy for the duration of exposure; Fig. 8) may be used to constrain the ^{81}Kr/^{78}Kr$_{it}$ production ratio. Using the two samples from Mud Tank with the highest ^{81}Kr/^{78}Kr$_{it}$ ratio for exposures >200 kyr (MUD-1 & MUD-11), we constrain the ^{81}Kr/^{78}Kr$_{it}$ production ratio to be 1.94±0.09 (1 SE; error weighted mean). The ^{81}Kr/^{78}Kr$_{it}$ production ratio derived from proton irradiation experiments is ~15% higher (for $\geq$ 49.2 g cm^{-2} shielding, ^{81}Kr/^{78}Kr$_{it}$ = 2.30±0.02, 1SD; Table 2a of Gilabert et al. 2002). This difference may be due to unaccounted for episodes of sample burial, or the inherently different reaction pathways and energy spectra in proton experiments (Gilabert et al., 2002) as compared to the secondary neutron flux at the Earth's Surface (Lifton et al., 2014). Using either production ratio, the results for all Mud Tank zircons analysed are consistent with the ^{81}Kr$_{it}$ production rate of 6.33±0.32 atoms g^{-1} yr^{-1} derived earlier and the ^{81}Kr half-life of 229±11 kyr (Baglin, 2008), assuming either a continuous exposure, a uniform erosion rate, or a complex exposure history (Fig. 8). In the following we use the ^{81}Kr/^{78}Kr$_{it}$ production ratio of 1.94±0.09.

4.4.1 Glacially exhumed samples

The results of the glacially exhumed samples from the Grimsel Pass area are consistent with a post-LGM (Last Glacial Maximum) exposure under a variable and significant snow cover (Wirsig et al., 2016). Grimsel Pass ^{81}Kr/^{78}Kr$_{it}$ values (1.33±0.25, 1.35±0.30 and 2.00±0.79; 1 SE, error weighted mean; Fig. 8) are consistent with the production ratio derived from the Mud Tank zircons within two standard errors (1.94±0.09; 1 SE; see above), however, two of three samples are inconsistent with the experimental value (2.3, see above). Irrespective of eventual intermittent cover, samples with no exposure prior to glacial erosion history (as is inferred for Grimsel Pass area, see section 2) should exhibit ^{81}Kr/^{78}Kr$_{it}$-ratios indistinguishable from the production ratio. The 40-50 % difference between the expected ^{81}Kr$_{it}$ concentrations at Grimsel Pass (commensurate to ~13 kyr exposure (Wirsig et al., 2016)) and those measured (Fig. 8) indicate a notable amount of seasonal snow cover at our sampling locations (Wirsig et al., 2016). The quartz-vein samples used by Wirsig et al. (2016) for exposure dating were collected on steep-sided outcrops to prevent significant snow-cover; our granite samples were from near-horizontal outcrops (Fig. 4) to ensure a simple exposure geometry of our large (~10 kg; in order to recover sufficient zircon) and thick samples (10 to 15 cm).
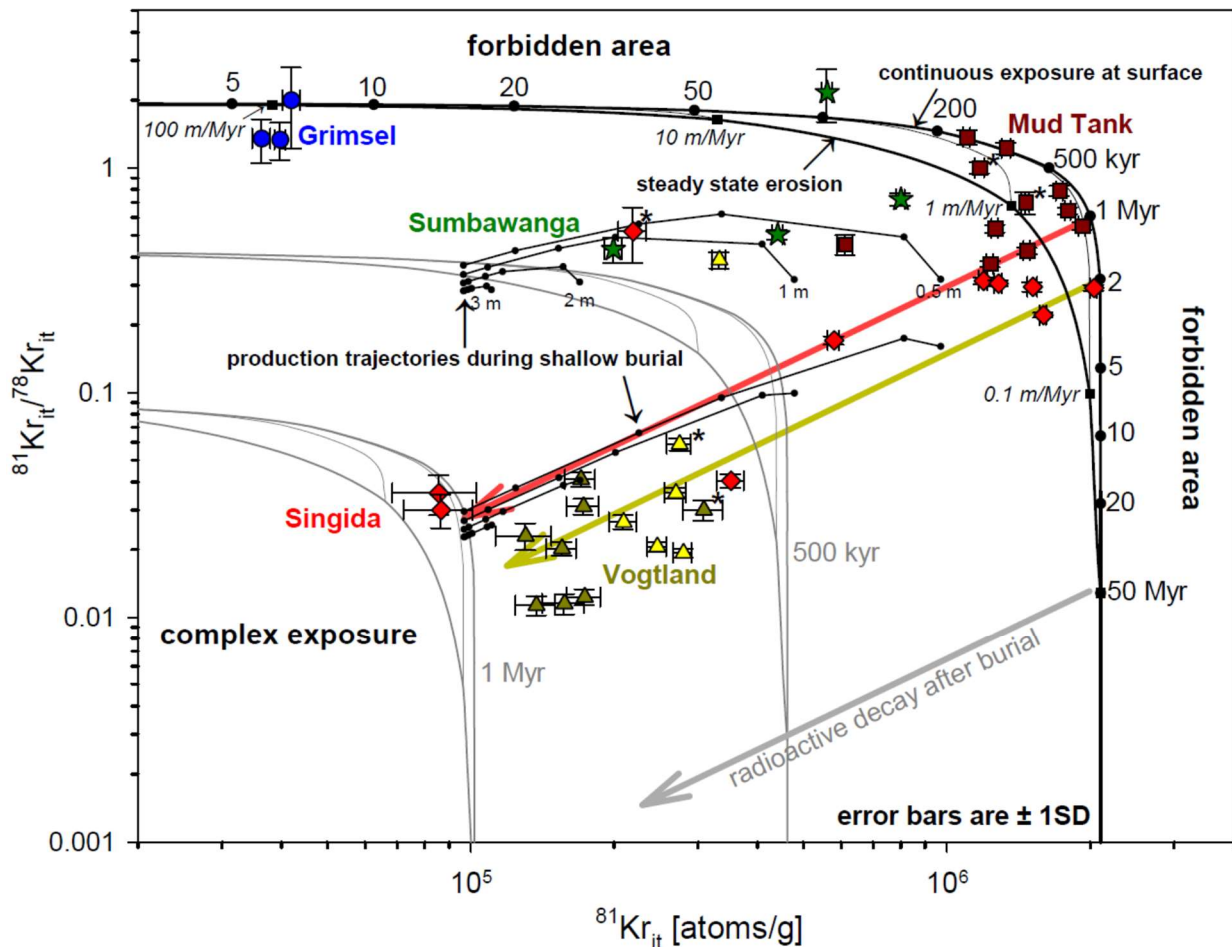
Figure 8. Unravelling histories of exposure and burial. In a $^{81}Kr/^{78}Kr_{it}$ vs. ^{81}Kr two-isotope plot, analogous to similar diagrams used for ^{26}Al and ^{10}Be (Dunai, 2010; Lal, 1991) or ^{21}Ne and ^{10}Be (Kober et al., 2009), histories of exposure and burial can be deciphered. The spallogenic $^{81}Kr/^{78}Kr_{it}$ production ratio (1.94 ± 0.09; 1SE calculated from samples MUD-1 & MUD-11; see main text), the $^{81}Kr_{it}$ production rate (6.33 ± 0.32 atoms g^{-1}yr^{-1}; this study) and the ^{81}Kr half-life (229 ± 11 kyr, Baglin, 2008) are used to define the boundaries between areas that are forbidden (no physically plausible explanation), areas that denote simple continuous exposure or steady state erosion, or complex histories that include intermittent burial. Samples that are continuously exposed at the surface may be used to test the consistency of the $^{81}Kr/^{78}Kr_{it}$ production ratio and/or $^{81}Kr_{it}$ production rate applied. Due do the decay of ^{81}Kr, the $^{81}Kr/^{78}Kr_{it}$ ratio of exposed samples decreases with increasing exposure age until the ^{81}Kr concentration eventually saturates (production rate = decay rate) after about 8 - 9 half-lives (this limit is dependent on the analytical uncertainties achieved). For exposures > 1 Myr, the $^{81}Kr_{it}/^{78}Kr_{it}$- ratio is a direct proxy for the exposure age (Marti, 1967), independent of scaling factors or shielding as long as the latter is constant through time (Marti, 1967). Upon burial the previously acquired $^{81}Kr_{it}$ inventory decays over time, allowing, in the case of a single period of deep burial, its duration to be determined. All samples are consistent with either continuous exposure at the Earth's surface, exhumation at a steady rate, or with histories that include burial after exposure ('complex exposure'). Samples marked with an asterisk (*) are those that were identified to contain fractionated and/or nucleogenic Kr (Fig. 7); results of these samples are excluded from further evaluation. The two colours used for the samples from Vogtland denote the distance they were collected downstream of their source (yellow ~5 km; dark yellow ~15 km). Symbols and colours for samples are

the same as in Figure 6. For two samples from Grimsel (GRIM-19-1 & 2) the error weighted means (1SE) of

duplicate/triplicate measurements are plotted. The $^{81}Kr_{it}$ concentrations are normalized to sea-level and high-

latitude using LSD scaling (Lifton et al., 2014), and the standard atmosphere model to convert altitude into

atmospheric pressure (Balco et al., 2008). The evolution trajectories shown are calculated using a $^{81}Kr_{it}/^{78}Kr_{it}$

production ratio of 1.94 (this study), a sea-level high-latitude $^{81}Kr_{it}$ production rate of 6.33 (this study), the $^{81}Kr_{it}$

half-life of 229 kyr (Baglin, 2008), and a density of 2.7 g cm^{-3} for source rocks and/or overburden. Format of

diagram after Lal (1991). The two, subordinate, steady-state erosion islands bound by the grey lines give

hypothetical examples of where samples would plot had they been originally exposed at the surface and then

buried at a significant depth for 500 kyr, or for 1 Myr. The two sets of example production trajectories illustrate

regrowth at shallower depths (i.e., 3 m, 2 m, 1 m and 0.5 m; during 500 and 1000 kyr of burial, respectively).

Trajectories are vertically offset within each set for better visibility (i.e., the trajectories for the different burial

depths actually originate from one point). Dots on the regrowth trajectories are for 0 yr, 10 kyr, 50 kyr, 100 kyr,

500 kyr, and 1 Myr production, respectively.

536

4.4.2 Sedimentary samples

538 The sedimentary zircon megacrysts from Australia, Tansania and Germany have the ability to record

539 their individual (paleo-) exhumation and subsequent burial histories. Their exhumation rate is taken to

540 be representative of the erosion rates of their former host rocks (for simplicity we assume a 2.7 g cm^{-3}

541 density for all, which may not necessarily be the case). The simplest case is for zircons from Mud Tank

542 (Australia), since they were collected at or near the surface in close proximity to their source rock. The

543 sample results indicate individual exhumation rates between 1 m Myr^{-1} and 0.1 m Myr^{-1} (Fig. 8) and

544 that some zircons have had a complex exposure history, with intermittent burial and/or production at

545 shallow depths (Fig. 8). These results are consistent with erosion rates obtained for other low-relief,

546 post-orogenic landscapes in arid Central Australia (Struck et al., 2018b; Struck et al., 2018a) and with

547 being sampled at or near the surface of a thin sediment cover (Australian_Vermiculite_Industries, 2013;

548 Struck et al., 2018a).

549

550 A more complex history is implied for the zircons from the Singida peneplain (Tanzania, Mannard,

551 1962). The sediments of the ephemeral rivers from which they were mined commonly have a thickness

552 of several meters; thus, samples may record extended periods of burial. The samples from the Singida

553 form a pattern (n=9; Fig. 8) that is commensurate with exhumation rates lower than 0.1 m Myr^{-1} and

554 continuous exposure at the surface, or burial for to up to 1 Myr. These results from the Singida diatreme

555 field are consistent with expectations for an arid, low-relief (<50 m), long wavelength (> 10 km)

556 landscape (Mannard, 1962; Harrison et al., 2001), notionally a relic of Cretaceous age ('African Surface';

557 Mannard, 1962; King, 1978; Burke et al., 2008). The notion of long-term low erosion rates is supported

558 by the partial preservation of tuff-rings of Eocene diatremes (Mannard, 1962; Harrison et al., 2001),

559 with the tuffs being the source-rocks of the zircons (Mannard, 1962). The erosion rates we infer from the

560 zircons are very low (< 0.1 m Myr^{-1}), and appear to have been invariable during the last 1 Myr.

561 Assuming these rates apply to even longer time scales, the source of the zircons would have eroded by
562 less than 4.5 m since the eruption of the diatreme, 44.8±0.2 Myr ago (mean U-Pb ages of zircons; n=9,
563 1SD; Table 2).

564

565 The basic framework for zircons from Sumbawanga (Tanzania) is similar to Singida inasmuch as the
566 zircons were retrieved from river sediments but the surface process rates are different. The Precambrian
567 source rocks (Kabete et al., 2012) for zircons from Sumbawanga have experienced post Mid-Miocene
568 uplift and tectonic segmentation as part of the Tanganyika–Rukwa–Malawi transform-segment of the
569 East African Rift segments (Chorowicz, 2005). The resulting localized, short wavelength (1-8 km) relief
570 is in places significant (up to 600 m). The current local climate is temperate (Peel et al., 2007), rather
571 than arid. The samples from Sumbuwanga (Fig. 8) indicate individual exhumation rates around 1 m
572 Myr^{-1} and all but one have had a complex exposure history, with burial for up to 500 kyr and/or
573 production at shallow depths. The order of magnitude higher erosion rates inferred for source regions of
574 Sumbawanga zircons, as compared to Singida, are commensurate with the different tectonomorphology
575 and climatic conditions.

576

577 The setting of the samples from the Vogtland (Germany) is distinct from the other sedimentary samples
578 in this study as it is the only location that experienced periglacial conditions in the past (Eissmann,
579 2002). The area was never glaciated but was within 50 km of the ice-margins during the largest
580 Quaternary glaciations (Eissmann, 2002). The climate is currently temperate (Bohn and Gollub, 2006;
581 Kreklow et al., 2019). The relief is moderate, at 200 - 300 m over 2 - 3 km scale wavelengths. The
582 zircons' source is a kimberlitic diatreme (Schmidt et al., 2013; Modalek et al., 2009) that intruded into
583 Palaeozoic slates 71.2 ± 0.8 Myr ago (U-Pb age; Table 2). The diatreme acts as the headwaters of the
584 drainage system investigated. The zircons from the Vogtland form a cluster (n = 13; Fig. 8) that is
585 commensurate with a long (1 to 3 Myr) exposure at or near the surface, or exhumation at a very low rate
586 (< 0.1 m Myr^{-1}), followed by a period of burial for 600 to 900 kyr and a recent re-emergence in the
587 active fluvial system. Samples collected further from the source (15 vs. 5 km) appear to have longer
588 burial histories (Fig. 8). The extremely low erosion rates inferred for exposure prior to burial (< 0.1 m
589 Myr^{-1}) are unprecedented for temperate regions in Europe and late Quaternary erosion rates of similar
590 moderate relief landscapes are two orders of magnitude faster (> 10 m Myr^{-1}; (Schaller et al., 2001)).

591

592 The termination of the initial, long exposure of the Vogtland zircons ~900 kyr ago, coincides with the
593 marked climatic shifts associated with the '0.9 Ma event' (Marine Isotope Stage 22 (MIS 22); (Head and
594 Gibbard, 2015; Mcclymont et al., 2013; Lisiecki and Raymo, 2005)) during the Mid Pleistocene
595 Transition (MPT)(Clark et al., 2006; Head and Gibbard, 2005; Mcclymont et al., 2013). In Europe this
596 climatic shift is associated with pronounced acceleration of river incision (Gibbard and Lewin, 2009), in

part driven by increased sediment loads from periglacial hillslope processes (Gibbard and Lewin, 2009; Goodfellow and Boelhouwers, 2013). Until the Pleistocene, low-relief landscapes dominated throughout Europe (Gibbard and Lewin, 2009; Muttoni et al., 2003; Haeuselmann et al., 2007). This stasis came to an end during the MPT (Gibbard and Lewin, 2009; Muttoni et al., 2003; Haeuselmann et al., 2007), with a step change during MIS 22 (Gibbard and Lewin, 2009; Muttoni et al., 2003). The following, first major glaciation was MIS 16 (676 to 621 kyr; (Lisiecki and Raymo, 2005; Ehlers and Gibbard, 2007)), which overlaps with the youngest burial ages of zircons in the cluster (Fig. 8). One zircon from this group may record a shorter burial, or significant post-burial production at a shallower depth.

From the external constraints on climate and landscape evolution in Europe (Gibbard and Lewin, 2009; Head and Gibbard, 2015; Mcclymont et al., 2013; Pena and Goldstein, 2014) and our results (Fig. 8) we assemble the following, preliminary, scenario. A formerly stable Plio-Pleistocene landscape (Gibbard and Lewin, 2009) is exposed for the first time to periglacial conditions during MIS 22 (Head and Gibbard, 2015; Pena and Goldstein, 2014). A functional vegetation cover is largely lost and periglacial hillslope processes accelerate sediment supply (Gibbard and Lewin, 2009; Goodfellow and Boelhouwers, 2013). The ensuing surge in sediment supply may have overwhelmed the transport capabilities of low-order catchments and consequently sediments are stored on hillslopes or in the fluvial system. In the studied case, slopes would begin to be stripped of their pre-existing regolith cover during MIS 22 and this would have been largely concluded by the end of MIS 16. The finding that the burial ages of the zircons seem to increase with distance from their source locations points to a long-term burial in fluvial sediments, rather than in colluvium proximal to their source. Analyses of additional material and locations are currently ongoing to test this preliminary scenario. For the purpose of this study, we note that Kr_{it} is suitable to illuminate (Mid-) Pleistocene histories of burial and exposure.

5 Discussion

Our results from the suite of zircon samples taken from near-surface sediments and bedrock demonstrate the feasibility and utility of Kr_{it} for Earth surface science applications. Not all Kr isotopes are equally suitable for this purpose and some aspects concerning the main target mineral, zircon, need consideration. In the following, we elucidate these topics, outline the required research to address current limitations and explore the potential of this novel tool for Earth surface sciences.

5.1 The utility of Kr isotopes for cosmogenic applications

The utility for each of the various Kr_{it} isotopes is set by its relative abundance, the presence or absence of alternative production pathways (fissiogenic and/or nucleogenic), its half-life (where applicable) and its atmospheric abundance (^{80}Kr 2.25%; ^{82}Kr 11.6%; ^{83}Kr 11.5%; ^{84}Kr 57.0%; ^{86}Kr 17.3%; ^{78}Kr 0.35%;

633   [81]Kr 0.5 ppt; (Buizert et al., 2014; Aregbe et al., 1996)), i.e., its ubiquitous general background.

634   Specifically:

635

636   a) ^{78}Kr and ^{81}Kr are exclusively produced by cosmic rays, not by fission or nucleogenic reactions and

637   they are the rarest Kr isotopes in air (0.35% and 0.5 ppt in air; Fig. 1; (Buizert et al., 2014; Aregbe et al.,

638   1996). These factors facilitate the detection and quantification of small amounts of Kr$_{it}$.

639   b) ^{80}Kr and ^{82}Kr may be produced by nucleonic reactions on bromine,^{79}Br(n, γ)^{80}Kr, ^{81}Br(n, γ)^{82}Kr.

640   Reaction cross sections for thermal neutrons are 10.32 and 2.36 barn, respectively (Soppera et al.,

641   2014). Bromine concentrations are low in silicate minerals (Ruzie-Hamilton et al., 2016; Kendrick,

642   2012; Teiber et al., 2015) but often not constrained. The fissiogenic production of ^{82}Kr is negligible

643   (Fig. 1; (Jaea)). The presence of Kr$_{nuc}$ can be verified and affected samples can be excluded from further

644   interpretation (Fig. 7).

645   c) ^{83}Kr, which in meteorite studies is used as the most prominent Kr$_{iet}$ isotope, may be produced by

646   fission of ^{238}U (Fig. 1; (Eikenberg et al., 1993; Honda et al., 2004; Jaea)). Fissiogenic ^{83}Kr in zircon can

647   be appreciable, since zircon is commonly enriched in uranium (particularly in comparison with

648   meteorites) and Kr$_{fis}$ will accumulate over the geological age of zircons (Eikenberg et al., 1993; Honda

649   et al., 2004). Consequently, ^{83}Kr$_{it}$ may not be quantified or used with the same ease as in meteorite

650   studies.

651   d) Spallogenic production of ^{84}Kr and ^{86}Kr is (very) low compared to the other isotopes (Fig. 1; Gilabert

652   et al., 2002) and their fissiogenic production rates are highest (Fig. 1; Eikenberg et al., 1993; Jaea),

653   limiting their utility as cosmogenic nuclides.

654   e) Finally, the very short half-life of ^{85}Kr (t$_{½}$ = 10.7 yr; Lerner, 1963) renders this isotope less suited to

655   Earth surface science applications, though there may be interesting applications that could benefit from

656   this. However, concentrations of ^{85}Kr$_{it}$ will be fiendishly low, as it approaches saturation in as little as

657   ~50 years.

658

659   From the above (a to e) it follows that ^{78}Kr$_{it}$, ^{80}Kr$_{it}$, ^{81}Kr$_{it}$ and ^{82}Kr$_{it}$ are probably the most useful Kr$_{it}$

660   isotopes for Earth surface science applications. Having three stable isotopes allows the separation of

661   atmospheric, nucleogenic and fractionated components from cosmogenic Kr (Fig. 7). Fissiogenic

662   production can be neglected (^{82}Kr) or excluded (^{78,80,81}Kr) for all four nuclides (Fig. 1). Finally, ^{81}Kr$_{it}$ has

663   no interference by any geochemical component (Fig. 1) and has a rather useful half-life (t$_{½}$=229±11 kyr;

664   (Baglin, 2008)) for Earth surface science applications (Fig. 8).

665

666   Kr$_{it}$ is unique amongst the cosmogenic nuclides in that it has one long-lived radioactive (^{81}Kr) and

667   several suitable stable isotopes (Gilabert et al., 2002; Marti, 1967). As heavy residues of their target

668   nuclei, Kr$_{it}$ isotopes are not ejected from the target mineral, nor are they implanted from surrounding

669 material, as is the case for cosmogenic ^{3}He (Dunai, 2010; Dunai et al., 2007; Larsen et al., 2019). ^{78}Kr$_{it}$

670 is the only stable cosmogenic nuclide that cannot be produced by processes other than cosmogenic

671 production during the geological life-time of a rock, as its geochemical sources are gases of atmospheric

672 composition, unaltered since the accretion of Earth (Trieloff et al., 2000). The absence of significant

673 muogenic pathways of Kr production from Zr-isotopes (see Sect. 1.2.2) help facilitate its use in Earth

674 science applications.

675

676 **5.2 Zircon as target mineral**

677 Zircon is ubiquitous in igneous rocks and clastic sediments, occurring in granites as well as basalts

678 (Grimes et al., 2007; Samson et al., 2018; Keller et al., 2017). Zircon abundance in igneous rocks is

679 usually limited by the availability of zirconium, which has an average concentration of 82 ppm in the

680 oceanic crust (Jenner and O'neill, 2012) and of 193 ppm in the continental crust (Taylor and Mclennan,

681 1985). Taking 193 ppm Zr as a guide, the average continental crust may contain 390 ppm zircon. While

682 many granitoid rocks have zirconium/zircon concentrations close to the continental average, some might

683 deviate significantly (Keller et al., 2017). Zircon is amongst the most weathering-resistant minerals and

684 can survive the weathering-erosion-sedimentation-metamorphism-melting cycle of rocks (Hoskin and

685 Schaltegger, 2003; Belousova et al., 2002).

686

687 Zircon ($ZrSiO_4$) forms a continuous mixture series with hafnon ($HfSiO_4$). In most rocks, however, the

688 range in Hf-concentrations actually observed in zircon is small: 1.5 ± 1 wt % (Hoskin and Schaltegger,

689 2003; Belousova et al., 2002; Owen, 1987). Only highly evolved rocks, such as pegmatites, syenites or

690 carbonatites, may show significantly higher Hf-concentrations (Hoskin and Schaltegger, 2003;

691 Belousova et al., 2002). Since Hf does not contribute to Kr$_{it}$-production, its role in the target chemistry

692 would need consideration (Hf 'dilutes' the Zr) when interpreting Kr$_{it}$- concentrations in zircons from

693 such evolved rocks. Combined, all other impurities in zircon are well below the %-level (Hoskin and

694 Schaltegger, 2003; Belousova et al., 2002), thus need no consideration when interpreting Kr$_{it}$ -

695 concentrations. Hence, in most geological contexts where zircon might be used for cosmogenic

696 methodology, a composition of 98.5 ± 1 % $ZrSiO_4$ may safely be assumed (Hoskin and Schaltegger,

697 2003; Belousova et al., 2002; Owen, 1987), without performing a chemical assay.

698

699 Retention of noble gases in zircon is very good (Honda et al., 2004; Farley, 2007). The closure

700 temperatures for noble gases in zircon increase with increasing atomic mass: ^{4}He (160-200 ºC; Reiners,

701 2005), ^{21}Ne (400 ± 50 ºC; Gautheron et al., 2006), ^{86}Kr (560-580 ºC; Honda et al., 2004), ^{136}Xe (660-750

702 ºC, Honda et al., 2004). This may be a mixed blessing for some applications of Kr$_{it}$. On one hand, the

703 excellent retentivity makes paleo-erosion rate studies in diagenetically altered to slightly

704 metamorphosed rocks feasible. On the other hand, potentially incomplete resetting of the (stable) Kr$_{it}$ by

thermal diffusion in source rocks might complicate applications such as burial dating (Dunai, 2010). In any case, the retentivity of Kr_{it} under environmental conditions will be complete in structurally intact zircons. The qualifier 'structurally intact' is pointing to the fact that radioactivity within the zircon (α-decay of U, Th, Sm) causes cumulative radiation damage over time. This can eventually lead to complete destruction of the lattice and amorphization of the material (metamictization; (Ewing et al., 2003)). This process goes hand-in-hand with an increase in volume (lowering of density by up to 17%; (Ewing et al., 2003)). Retention of helium in zircon decreases at cumulative alpha doses above 10^{18} α g^{-1} (Guenthner et al., 2013; Reiners, 2005), zircon remains retentive for helium at environmental temperatures up to doses of $2\text{-}4\cdot10^{18}$ α g^{-1} (Reiners, 2005). Since retentivity of noble gases increases with atomic mass (see above), krypton will be retained quantitatively in zircon at environmental temperatures at least up to the dose of $2\text{-}4\cdot10^{18}$ α g^{-1}. A zircon with 1000 ppm U (with Th/U=0.5) requires ~10^9 years to receive a dose of $4\cdot10^{18}$ α g^{-1} (for a depiction of alpha dose as a function of age and U concentration we refer to (for a depiction of alpha dose as a function of age and U concentration we refer to Reiners, 2005). Thus, for most zircons, complete retentivity of krypton at environmental temperatures can be assumed. Evidence from other noble gases (Guenthner et al., 2013) and other minerals (Eikenberg et al., 1993; Ragettli et al., 1994) suggests that the retentivity of Kr_{it} may be an issue for highly metamict zircons. The glassy nature of highly metamict zircons also renders them more vulnerable to weathering (Ewing et al., 2011). However, it still takes intense tropical weathering (laterization) to (partially) destroy metamict zircons (Delattre et al., 2007).

5.3 Applications in the Earth sciences

Zircon as a target material stands out in terms of weathering resistance (Hoskin and Schaltegger, 2003; Belousova et al., 2002) and retentivity for noble gases (Honda et al., 2004; Farley, 2007). This combination of characteristics complements existing cosmogenic nuclide methodology (Dunai, 2010; Marti, 1967; Granger and Riebe, 2014; Gosse and Phillips, 2001). For instance, basin-wide denudation rates (Granger and Riebe, 2014) of lateritic regoliths, which cover large tracts of the Earth surface (e.g., (Burke et al., 2008)), and quartz-free lithologies such as basalts, which are important for CO_2 draw-down (Dessert et al., 2003), may be reliably addressed without the bias that is introduced when target minerals perish during weathering (Granger and Riebe, 2014). The additional information obtained by combining cosmogenic nuclides with different half-lives is inherently available, as the relevant Kr_{it} isotopes are measured simultaneously. The important detail that [78]Kr has no other sources than gases of atmospheric composition and cosmogenic production, allows, in principle, the determination of paleo-erosion rates from clastic sedimentary rocks of all ages.

The results presented here provide an idea of the utility of this new tool for dating changes of process rates on the Earth surface (MPT in temperate regions), or testing their notional long-term invariance

741 (African Surface). The ability to use stable/radionuclide pairs to track the exposure and burial history of

742 single grains of coarse sand or fine gravel helps to achieve this. However, amalgamated, multi-grain

743 samples for Kr_{it} are also possible and allow averaging approaches as are routinely available for other

744 cosmogenic nuclides (Granger and Riebe, 2014), with the added benefits of an inherent

745 stable/radionuclide pair and the unique weathering properties of zircon.

746

6 Conclusions

748 From this first study of in situ produced terrestrial krypton (Kr_{it}) we draw the following conclusions.

1. In situ produced cosmogenic krypton in terrestrial zircon can be analysed with the existing sector field mass spectrometry methodology. A high-resolution mass spectrometer aids resolving interferences from hydrocarbons and Ar_2H^+. Likewise, a low-blank laser-extraction of Kr from zircon aids resolving small isotopic enrichments relative to atmospheric Kr.

2. ^{78}Kr, ^{80}Kr, ^{81}Kr and ^{82}Kr are the most suitable Kr isotopes for terrestrial applications; this judgement is based on their abundance in air, the half-life of ^{81}Kr and the absence, or rarity of interfering geochemical components.

3. Cross-calibration to ^{10}Be-production in quartz ($^{81}Kr_{it}(zrc)/^{10}Be(qtz)=1.545\pm0.045$) yields a production rate of $^{81}Kr_{it}$ in zircon of 6.33 ± 0.32 atoms g^{-1} yr^{-1} at sea-level and high-latitude. Our measurements indicate a terrestrial $^{81}Kr/^{78}Kr_{it}$ production ratio in zircon of 1.94 ± 0.09 and that the air-spallogenic mixing line in $^{78}Kr/^{82}Kr$$^{80}Kr/^{82}Kr$ space (Fig. 7) has a slope of 1.682 ± 0.015 (uncertainties are 1SD).

4. As heavy residues of spallation, Kr_{it}-nuclei are neither implanted into zircon nor ejected from zircon. Hence, Kr_{it} production rates are not dependent on grain-size or matrix, as is the case for cosmogenic ^3He (Dunai, 2010; Larsen et al., 2019).

5. Interfering geochemical components and physical processes (fractionation) can be reliably identified using ^{78}Kr, ^{80}Kr and ^{82}Kr; similar to the existing methodology for cosmogenic neon (three-isotope diagram; Niedermann, 2002).

6. The combination of a stable Kr_{it}-isotope (here $^{78}Kr_{it}$) and radioactive $^{81}Kr_{it}$ ($t\frac{1}{2}$ = 229 kyr, Baglin, 2008) allows the reconstruction of complex histories of exposure and burial, similar to the existing methodology for ^{10}Be and ^{26}Al ('banana plot'; Lal, 1991). The shorter half-life of ^{81}Kr, as compared to ^{26}Al ($t\frac{1}{2}$ = 708 kyr, Nishiizumi, 2004) permits reconstructions of younger burial histories, as compared to existing methodology (i.e., combining ^{10}Be and ^{26}Al and assuming similar analytical uncertainties for equivalent exposure). The upper time-limit for resolving burial histories should be lower than 2 Myr, with the actual values of the upper and lower limits dependent on the analytical uncertainties.

775   7. In situations with a long, continuous exposure (> 1 Ma), ^{81}Kr-Kr ages, which are independent of
776   scaling, may be calculated using the existing methodology from meteoritics (Marti, 1967; Leya et
777   al., 2015).

778   8. ^{78}Kr has no sources other than gases of atmospheric composition and cosmogenic production,
779   allowing, in principle, the determination of paleo-erosion rates from clastic sedimentary rocks of all
780   ages.

781

782

Author contribution

TJD conceptualized the study and designed the noble gas experiments. Investigation and formal analysis of data was carried out by all authors. TJD prepared the manuscript with contributions from all co-authors.

Competing interests:

The authors declare that they have no conflict of interest.

29

805 **References**

806 Arblaster, J. W.: Thermodynamic Properties of Tantalum, Journal of Phase Equilibria
807 and Diffusion, 39, 255-272, 10.1007/s11669-018-0627-2, 2018.
808 Aregbe, Y., Valkiers, S., Mayer, K., and DeBievre, P.: Comparative isotopic
809 measurements on xenon and krypton, International Journal of Mass Spectrometry and
810 Ion Processes, 153, L1-L5, 10.1016/0168-1176(96)04368-6, 1996.
811 Australian_Vermiculite_Industries: Mine Closure Plan Mud Tank Operation MIN 165,
812 https://geoscience.nt.gov.au/gemis/ntgsjspui/bitstream/1/80230/3/MLS165_2014_AS_03_A
813 PPENDIX2_MCP.pdf, 2013.
814 Baglin, C. M.: Nuclear Data Sheets for A=81, Nuclear Data Sheets, 109, 2257-2437,
815 10.1016/j.nds.2008.09.001, 2008.
816 Balco, G.: Glacier Change and Paleoclimate Applications of Cosmogenic-Nuclide
817 Exposure Dating, Annual Review of Earth and Planetary Sciences, 48, 21-48,
818 10.1146/annurev-earth-081619-052609, 2020.
819 Balco, G., Stone, J. O., Lifton, N. A., and Dunai, T. J.: A complete and easily
820 accessible means of calculating surface exposure ages or erosion rates from Be-10
821 and Al-26 measurements, Quaternary Geochronology, 3, 174-195,
822 10.1016/j.quageo.2007.12.001, 2008.
823 Belousova, E. A., Griffin, W. L., O'Reilly, S. Y., and Fisher, N. I.: Igneous
824 zircon: trace element composition as an indicator of source rock type, Contributions
825 to Mineralogy and Petrology, 143, 602-622, 10.1007/s00410-002-0364-7, 2002.
826 Binnie, S. A., Dunai, T. J., Voronina, E., Goral, T., Heinze, S., and Dewald, A.:
827 Separation of Be and Al for AMS using single-step column chromatography, Nuclear
828 Instruments and Methods in Physics Research Section B: Beam Interactions with
829 Materials and Atoms, 2015.
830 Binnie, S. A., Dewald, A., Heinze, S., Voronina, E., Hein, A., Wittmann, H., von
831 Blanckenburg, F., Hetzel, R., Christl, M., Schaller, M., Leanni, L., Hippe, K.,
832 Vockenhuber, C., Ivy-Ochs, S., Maden, C., Fulop, R. H., Fink, D., Wilcken, K. M.,
833 Fujioka, T., Fabel, D., Freeman, S., Xu, S., Fifield, L. K., Akcar, N., Spiegel, C.,
834 Dunai, T. J., Aumaitre, G., Bourles, D. L., Keddadouche, K., and Team, A.:
835 Preliminary results of CoQtz-N: A quartz reference material for terrestrial in situ
836 cosmogenic Be-10 and Al-26 measurements, Nuclear Instruments & Methods in Physics
837 Research Section B-Beam Interactions with Materials and Atoms, 456, 203-212,
838 10.1016/j.nimb.2019.04.073, 2019.
839 Bohn, U. and Gollub, G.: The use and application of the map of the natural
840 vegetation of Europe with particular refernce to Germany, Biology and Environment:
841 Proceedings of the Royal Irish Academy, 106B, 199-213, 2006.
842 Broadley, M. W., Barry, P. H., Bekaert, D. V., Byrne, D. J., Caracausi, A.,
843 Ballentine, C. J., and Marty, B.: Identification of chondritic krypton and xenon in
844 Yellowstone gases and the timing of terrestrial volatile accretion, Proceedings of
845 the National Academy of Sciences of the United States of America, 117, 13997-14004,
846 10.1073/pnas.2003907117, 2020.
847 Buizert, C., Baggenstos, D., Jiang, W., Purtschert, R., Petrenko, V. V., Lu, Z. T.,
848 Muller, P., Kuhl, T., Lee, J., Severinghaus, J. P., and Brook, E. J.: Radiometric
849 Kr-81 dating identifies 120,000-year-old ice at Taylor Glacier, Antarctica,
850 Proceedings of the National Academy of Sciences of the United States of America,
851 111, 6876-6881, 10.1073/pnas.1320329111, 2014.
852 Burgess, R., Cartigny, P., Harrison, D., Hobson, E., and Harris, J.: Volatile
853 composition of microinclusions in diamonds from the Panda kimberlite, Canada:
854 Implications for chemical and isotopic heterogeneity in the mantle, Geochimica et
855 Cosmochimica Acta, 73, 1779-1794, https://doi.org/10.1016/j.gca.2008.12.025, 2009.
856 Burke, K., Gunnell, Y., Burke, K., and Gunnell, Y.: The African Erosion Surface: A
857 Continental-Scale Synthesis of Geomorphology, Tectonics, and Environmental Change
858 over the Past 180 Million Years, in: The African Erosion Surface: A Continental-
859 Scale Synthesis of Geomorphology, Tectonics, and Environmental Change over the Past
860 180 Million Years, Geological Society of America, 0, 10.1130/2008.1201, 2008.
861 Burnard, P., Zimmermann, L., and Sano, Y.: The Noble Gases as Geochemical Tracers:
862 History and Background, in: The Noble Gases as Geochemical Tracers, edited by:

30

Burnard, P., Springer Berlin Heidelberg, Berlin, Heidelberg, 1-15, 10.1007/978-3-642-28836-4_1, 2013.

Chorowicz, J.: The East African rift system, Journal of African Earth Sciences, 43, 379-410, https://doi.org/10.1016/j.jafrearsci.2005.07.019, 2005.

Clark, P. U., Archer, D., Pollard, D., Blum, J. D., Rial, J. A., Brovkin, V., Mix, A. C., Pisias, N. G., and Roy, M.: The middle Pleistocene transition: characteristics, mechanisms, and implications for long-term changes in atmospheric pCO2, Quaternary Science Reviews, 25, 3150-3184, 2006.

Crohn, P. W. and Moore, D. H.: The Mud Tank carbonatite, Strangways Range, Central Australia, Bmr Journal of Australian Geology & Geophysics, 9, 13-18, 1984.

Currie, K. L., Knutson, J., and Temby, P. A.: The Mud Tank carbonatite complex, Central Australia - An example of metasomatism at midcrustal levels, Contributions to Mineralogy and Petrology, 109, 326-339, 10.1007/bf00283322, 1992.

Delattre, S., Utsunomiya, S., Ewing, R. C., Boeglin, J. L., Braun, J. J., Balan, E., and Calas, G.: Dissolution of radiation-damaged zircon in lateritic soils, American Mineralogist, 92, 1978-1989, 10.2138/am.2007.2514, 2007.

Dessert, C., Dupré, B., Gaillardet, J., François, L. M., and Allègre, C. J.: Basalt weathering laws and the impact of basalt weathering on the global carbon cycle, Chemical Geology, 202, 257-273, https://doi.org/10.1016/j.chemgeo.2002.10.001, 2003.

Dewald, A., Heinze, S., Jolie, J., Zilges, A., Dunai, T., Rethemeyer, J., Melles, M., Staubwasser, M., Kuczewski, B., Richter, J., Radtke, U., von Blanckenburg, F., and Klein, M.: CologneAMS, a dedicated center for accelerator mass spectrometry in Germany, Nuclear Instruments & Methods in Physics Research Section B-Beam Interactions with Materials and Atoms, 294, 18-23, 10.1016/j.nimb.2012.04.030, 2013.

Dunai, T. J.: Cosmogenic Nuclides: Principles, concepts and applications in the Earth surface sciences, Cambridge University Press2010.

Dunai, T. J., Stuart, F. M., Pik, R., Burnard, P., and Gayer, E.: Production of He-3 in crustal rocks by cosmogenic thermal neutrons, Earth and Planetary Science Letters, 258, 228-236, 10.1016/j.espl.2007.03.031, 2007.

Ehlers, J. and Gibbard, P. L.: The extent and chronology of Cenozoic Global Glaciation, Quaternary International, 164-165, 6-20, https://doi.org/10.1016/j.quaint.2006.10.008, 2007.

Eikenberg, J., Signer, P., and Wieler, R.: U-Xe, U-Kr, and U-Pb systematics for uranium minerals and investigations of the production of nucleogenic neon and argon, Geochim. Cosmochim. Acta., 57, 1053-1069, 1993.

Eissmann, L.: Quaternary geology of eastern Germany (Saxony, Saxon–Anhalt, South Brandenburg, Thüringia), type area of the Elsterian and Saalian Stages in Europe, Quaternary Science Reviews, 21, 1275-1346, https://doi.org/10.1016/S0277-3791(01)00075-0, 2002.

Ewing, R. C., Haaker, R. F., and Lutze, W.: Leachability of Zircon as a Function of Alpha Dose, MRS Online Proceedings Library, 11, 389, 10.1557/PROC-11-389, 2011.

Ewing, R. C., Meldrum, A., Wang, L. M., Weber, W. J., and Corrales, L. R.: Radiation effects in zircon, in: Zircon, edited by: Hanchar, J. M., and Hoskin, P. W. O., Reviews in Mineralogy & Geochemistry, 387-425, 10.2113/0530387, 2003.

Farley, K. A.: He diffusion systematics in minerals: Evidence from synthetic monazite and zircon structure phosphates, Geochim. Cosmochim. Acta, 71, 4015-4052, 2007.

Gain, S. E. M., Greau, Y., Henry, H., Belousova, E., Dainis, I., Griffin, W. L., and O'Reilly, S. Y.: Mud Tank Zircon: Long-Term Evaluation of a Reference Material for U-Pb Dating, Hf-Isotope Analysis and Trace Element Analysis, Geostandards and Geoanalytical Research, 43, 339-354, 10.1111/ggr.12265, 2019.

Gautheron, C. E., Tassan-Got, L., and Farley, K. A.: (U–Th)/Ne chronometry, Geochimica et Cosmochimica Acta, 70, A196, https://doi.org/10.1016/j.gca.2006.06.395, 2006.

Gerdes, A. and Zeh, A.: Zircon formation versus zircon alteration – New insights from combined U–Pb and Lu–Hf in-situ LA-ICP-MS analyses, and consequences for the interpretation of Archean zircon from the Central Zone of the Limpopo Belt, Chemical Geology, 261, 230-243, https://doi.org/10.1016/j.chemgeo.2008.03.005, 2009.

Gibbard, P. L. and Lewin, J.: River incision and terrace formation in the Late
Cenozoic of Europe, Tectonophysics, 474, 41-55,
https://doi.org/10.1016/j.tecto.2008.11.017, 2009.

Gilabert, E., Lavielle, B., Michel, R., Leya, I., Neumann, S., and Herpers, U.:
Production of krypton and xenon isotopes in thick stony and iron targets
isotropically irradiated with 1600 MeV protons, Meteoritics & Planetary Science, 37,
951-976, 10.1111/j.1945-5100.2002.tb00869.x, 2002.

Goodfellow, B. and Boelhouwers, J.: Hillslope Processes in Cold Environments : An
illustration of High Latitude Hillslope Processes and Forms, in: Treatise of
Geomorphology, edited by: John, F. S., Elsevier, 320-336, 2013.

Gosse, J. C. and Phillips, F. M.: Terrestrial in situ cosmogenic nuclides: theory
and application, Quat. Sci. Rev., 20, 1475-1560, 2001.

Granger, D. E. and Riebe, C. S.: 7.12 - Cosmogenic Nuclides in Weathering and
Erosion, in: Treatise on Geochemistry (Second Edition), edited by: Holland, H. D.,
and Turekian, K. K., Elsevier, Oxford, 401-436, https://doi.org/10.1016/B978-0-08-
095975-7.00514-3, 2014.

Grimes, C. B., John, B. E., Kelemen, P. B., Mazdab, F. K., Wooden, J. L., Cheadle,
M. J., Hanghoj, K., and Schwartz, J. J.: Trace element chemistry of zircons from
oceanic crust: A method for distinguishing detrital zircon provenance, Geology, 35,
643-646, 10.1130/g23603a.1, 2007.

Guenthner, W. R., Reiners, P. W., Ketcham, R. A., Nasdala, L., and Giester, G.:
Helium diffusion in natural zircon: radiation damage, anisotropy, and the
interpretation of zircon (U-Th)/He thermochronology, American Journal of Science,
313, 145-198, 10.2475/03.2013.01, 2013.

Haeuselmann, P., Granger, D. E., Jeannin, P. Y., and Lauritzen, S. E.: Abrupt
glacial valley incision at 0.8 Ma dated from cave deposits in Switzerland, Geology,
35, 143-146, 2007.

Harrison, T., Msuya, C. P., Murray, A. M., Jacobs, B. F., Báez, A. M., Mundil, R.,
and Ludwig, K. R.: Paleontological Investigations at the Eocene Locality of Mahenge
in North-Central Tanzania, East Africa, in: Eocene Biodiversity: Unusual Occurrences
and Rarely Sampled Habitats, edited by: Gunnell, G. F., Springer US, Boston, MA, 39-
74, 10.1007/978-1-4615-1271-4_2, 2001.

Head, M. J. and Gibbard, P. L.: Early-middle Pleistocene transitions: the land-ocean
evidence, Geol. Soc. Spec. Publ., 247, 1-18, 2005.

Head, M. J. and Gibbard, P. L.: Early–Middle Pleistocene transitions: Linking
terrestrial and marine realms, Quaternary International, 389, 7-46,
https://doi.org/10.1016/j.quaint.2015.09.042, 2015.

Hettmann, K., Siebel, W., Spiegel, C., and Reinecker, J.: Granite genesis and
migmatization in the western Aar Massif, Switzerland, Neues Jahrbuch Fur
Mineralogie-Abhandlungen, 186, 309-320, 10.1127/0077-7757/2009/0150, 2009.

Hoch, M., Nakata, M., and Johnson, H. L.: Vapor pressure of inorganic substances.
XII. Zirconium Dioxide, J. Am. Soc., 76, 2651-2652, 1954.

Honda, M., Nutman, A. P., Bennett, V. C., and Yatsevich, I.: Radiogenic, nucleogenic
and fissiogenic noble gas compositions in early Archaean magmatic zircons from
Greenland, Geochemical Journal, 38, 265-269, 10.2343/geochemj.38.265, 2004.

Hoskin, P. W. O. and Schaltegger, U.: The composition of zircon and igneous and
metamorphic petrogenesis, in: Zircon, edited by: Hanchar, J. M., and Hoskin, P. W.
O., Reviews in Mineralogy & Geochemistry, 27-62, 10.2113/0530027, 2003.

JAEA: JENDL FP Fission Yields Data File 2011 [dataset],
https://wwwndc.jaea.go.jp/cgi-bin/FPYfig, 2011.

Jenner, F. E. and O'Neill, H. S.: Analysis of 60 elements in 616 ocean floor
basaltic glasses, Geochemistry Geophysics Geosystems, 13, 10.1029/2011gc004009,
2012.

Kabete, J. M., Groves, D. I., McNaughton, N. J., and Mruma, A. H.: A new tectonic
and temporal framework for the Tanzanian Shield: Implications for gold metallogeny
and undiscovered endowment, Ore Geology Reviews, 48, 88-124,
10.1016/j.oregeorev.2012.02.009, 2012.

Kaiser, A., Lobert, M., and Telle, R.: Thermal stability of zircon (ZrSiO4), Journal of the European Ceramic Society, 28, 2199-2211, https://doi.org/10.1016/j.jeurceramsoc.2007.12.040, 2008.

Kamenetsky, V. S., Golovin, A. V., Maas, R., Giuliani, A., Kamenetsky, M. B., and Weiss, Y.: Towards a new model for kimberlite petrogenesis: Evidence from unaltered kimberlites and mantle minerals, Earth-Science Reviews, 139, 145-167, https://doi.org/10.1016/j.earscirev.2014.09.004, 2014.

Kaneoka, I.: Rare gas isotopes and mass fractionation: an indicator of gas transport into or from a magma, Earth and Planetary Science Letters, 48, 284-292, 1980.

Keller, C. B., Boehnke, P., and Schoene, B.: Temporal variation in relative zircon abundance throughout Earth history, Geochemical Perspectives Letters, 3, 179-189, 10.7185/geochemlet.1721, 2017.

Kendrick, M. A.: High precision Cl, Br and I determinations in mineral standards using the noble gas method, Chemical Geology, 292, 116-126, 10.1016/j.chemgeo.2011.11.021, 2012.

King, L.: The geomorphology of central and southern Africa, in: Biogeography and Ecology of Southern Africa, edited by: Werger, M. J. A., Springer Netherlands, Dordrecht, 1-17, 10.1007/978-94-009-9951-0_1, 1978.

Kober, F., Ivy-Ochs, S., Zeilinger, G., Schlunegger, F., Kubik, P. W., Baur, H., and Wieler, R.: Complex multiple cosmogenic nuclide concentration and histories in the arid Rio Lluta catchment, northern Chile, Earth Surface Processes and Landforms, 34, 398-412, 10.1002/esp.1748, 2009.

Kohl, C. and Nishiizumi, K.: Chemical isolation of quartz for measurement of in-situ-produced cosmogenic nuclides, Geochimica et Cosmochimica Acta, 56, 3583-3587, 1992.

Kreklow, J., Tetzlaff, B., Kuhnt, G., and Burkhard, B.: A Rainfall Data Intercomparison Dataset of RADKLIM, RADOLAN, and Rain Gauge Data for Germany, Data, 4, 118, 2019.

Lal, D.: Cosmic ray labeling of erosion surfaces: in situ nuclide production rates and erosion models, Earth Planet. Sci. Lett., 104, 424-439, 1991.

Larsen, I. J., Farley, K. A., and Lamb, M. P.: Cosmogenic 3He production rate in ilmenite and the redistribution of spallation 3He in fine-grained minerals, Geochimica et Cosmochimica Acta, 265, 19-31, https://doi.org/10.1016/j.gca.2019.08.025, 2019.

Lerner, J.: Half-life of 85Kr, Journal of Inorganic and Nuclear Chemistry, 25, 749-757, https://doi.org/10.1016/0022-1902(63)80357-7, 1963.

Leya, I., Gilabert, E., Lavielle, B., Wiechert, U., and Wieler, R.: Production rates for cosmogenic krypton and argon isotopes in H-Chondrites with known ^{36}Cl-^{36}Ar ages, Antarct. Meteorite Res., 17, 185-199, 2004.

Leya, I., Dalcher, N., Vogel, N., Wieler, R., Caffee, M. W., Welten, K. C., and Nishiizumi, K.: Calibration of cosmogenic noble gas production based on Cl-36-Ar-36 ages. Part 2. The Kr-81-Kr dating technique, Meteoritics & Planetary Science, 50, 1863-1879, 10.1111/maps.12515, 2015.

Lifshitz, M. and Singer, P.: Nuclear excitation function and particle emission from complex nuclei following muon capture, Physical Review C, 22, 2135-2150, 10.1103/PhysRevC.22.2135, 1980.

Lifton, N., Sato, T., and Dunai, T. J.: Scaling in situ cosmogenic nuclide production rates using analytical approximations to atmospheric cosmic-ray fluxes, Earth and Planetary Science Letters, 386, 149-160, 10.1016/j.epsl.2013.10.052, 2014.

Lisiecki, L. E. and Raymo, M. E.: A Pliocene-Pleistocene stack of 57 globally distributed benthic δ18O records, Paleoceanography, 20, 2005.

Ludwig, K. R.: User's manual for Isoplot 3.75, 2012.

Mannard, G. W.: The Geology of the Singida Kimberlite Pipes, Tanganyika, Geological Sciences, McGill University, Montreal, 377 pp., 1962.

Marti, K.: Mass-spectrometric detection of cosmic-ray-produced ^{81}Kr in meteorites and possiblity of Kr-Kr dating, Physical Review Letters, 18, 264-&, 10.1103/PhysRevLett.18.264, 1967.

1035 Marti, K., Eberhardt, P., and Geiss, J.: Spallation, fission and neutron capture
1036 anomalies in meteoritic Krypton and Xenon, Zeitschrift Fur Naturforschung Part a-
1037 Astrophysik Physik Und Physikalische Chemie, A 21, 398-+, 1966.
1038 Martin, L. C. P., Blard, P. H., Balco, G., Lave, J., Delunel, R., Lifton, N., and
1039 Laurent, V.: The CREp program and the ICE-D production rate calibration database: A
1040 fully parameterizable and updated online tool to compute cosmic ray exposure ages,
1041 Quaternary Geochronology, 38, 25-49, 10.1016/j.quageo.2016.11.006, 2017.
1042 Mason, B., Nelon, J. A., Muir, P., and Taylor, S. R.: The compostion of the
1043 Chassigny meteorite, Meteoritics, 11, 21-27, https://doi.org/10.1111/j.1945-
1044 5100.1976.tb00311.x, 1976.
1045 McClymont, E. L., Sosdian, S. M., Rosell-Melé, A., and Rosenthal, Y.: Pleistocene
1046 sea-surface temperature evolution: Early cooling, delayed glacial intensification,
1047 and implications for the mid-Pleistocene climate transition, Earth-Science Reviews,
1048 123, 173-193, https://doi.org/10.1016/j.earscirev.2013.04.006, 2013.
1049 Measday, D. F.: The nuclear physics of muon capture, Physics Reports-Review Section
1050 of Physics Letters, 354, 243-409, 10.1016/s0370-1573(01)00012-6, 2001.
1051 Modalek, W., Seifert, G., and Weiß, S.: Edle Zirkone aus dem Sächsischen Vogtland,
1052 Lapis, 34, 13-26, 2009.
1053 Muttoni, G., Carcano, C., Garzanti, E., Ghielmi, M., Piccin, A., Pini, R., Rogledi,
1054 S., and Sciunnach, D.: Onset of major Pleistocene glaciations in the Alps, Geology,
1055 31, 989-992, 10.1130/g19445.1, 2003.
1056 Niedermann, S.: Cosmic-ray-produced noble gases in terrestrial rocks: dating tools
1057 for surface processes, Reviews in Mineralogy and Geochemistry, 47, 731-784, 2002.
1058 Niedermann, S., Schaefer, J. M., Wieler, R., and Naumann, R.: The production of
1059 cosmogenic ^{38}Ar from calcium in terrestrial pyroxene, Earth Planet. Sci. Lett., 257,
1060 596-608, 2007.
1061 Nishiizumi, K.: Preparation of 26 Al AMS standards, Nuclear Instruments and Methods
1062 in Physics Research Section B: Beam Interactions with Materials and Atoms, 223, 388-
1063 392, 2004.
1064 Nishiizumi, K., Imamura, M., Caffee, M. W., Southon, J. R., Finkel, R. C., and
1065 McAninch, J.: Absolute calibration of Be-10 AMS standards, Nucl. Instr. Meth. Phys.
1066 Res. B, 258, 403-413, 2007.
1067 Oostingh, K. F., Jourdan, F., Danisik, M., and Evans, N. J.: Advancements in
1068 cosmogenic Ar-38 exposure dating of terrestrial rocks, Geochimica Et Cosmochimica
1069 Acta, 217, 193-218, 10.1016/j.gca.2017.07.043, 2017.
1070 Owen, M. R.: Hafnium content of detrital zircons, a new tool for provenance study,
1071 Journal of Sedimentary Petrology, 57, 824-830, 1987.
1072 Peel, M. C., Finlayson, B. L., and McMahon, T. A.: Updated world map of the Köppen-
1073 Geiger climate classification, Hydrol. Earth Syst. Sci., 11, 1633-1644,
1074 10.5194/hess-11-1633-2007, 2007.
1075 Pena, L. D. and Goldstein, S. L.: Thermohaline circulation crisis and impacts during
1076 the mid-Pleistocene transition, Science, 345, 318-322, 10.1126/science.1249770,
1077 2014.
1078 Ragettli, R. A., Hebeda, E. H., Signer, P., and Wieler, R.: Uranium-xenon
1079 chronology: precise determination of λ_{sf*} ^{136}Y$_{sf}$ for spontaneous fission of ^{238}U, Earth
1080 Planet. Sci. Lett., 128, 653-670, 1994.
1081 Reiners, P. W.: Zircon (U-Th)/He Thermochronometry, Reviews in Mineralogy and
1082 Geochemistry, 58, 151-179, 10.2138/rmg.2005.58.6, 2005.
1083 Renne, P. R., Farley, K. A., Becker, T. A., and Sharp, W. D.: Terrestrial cosmogenic
1084 argon, Earth Planet. Sci. Lett., 188, 435-440, 2001.
1085 Ritter, B., Vogt, A., and Dunai, T. J.: Technical Note: Noble gas extraction
1086 procedure and performance of the Cologne Helix MC Plus multi-collector noble gas
1087 mass spectrometer for cosmogenic neon isotope analysis, Geochronology Discuss.,
1088 2021, 1-16, 10.5194/gchron-2021-11, 2021.
1089 Ruzie-Hamilton, L., Clay, P. L., Burgess, R., Joachim, B., Ballentine, C. J., and
1090 Turner, G.: Determination of halogen abundances in terrestrial and extraterrestrial
1091 samples by the analysis of noble gases produced by neutron irradiation, Chemical
1092 Geology, 437, 77-87, 10.1016/j.chemgeo.2016.05.003, 2016.

Saldanha, R., Back, H. O., Tsang, R. H. M., Alexander, T., Elliott, S. R., Ferrara, S., Mace, E., Overman, C., and Zalavadia, M.: Cosmogenic production of ^{39}Ar and ^{37}Ar in argon, Physical Review C, 100, 024608, 10.1103/PhysRevC.100.024608, 2019.

Samson, S. D., Moecher, D. P., and Satkoski, A. M.: Inherited, enriched, heated, or recycled? Examining potential causes of Earth's most zircon fertile magmatic episode, Lithos, 314, 350-359, 10.1016/j.lithos.2018.06.015, 2018.

Schaller, M., von Blanckenburg, F., Hovius, N., and Kubik, P. W.: Large-scale erosion rates from in situ produced cosmogenic nuclides in European river sediments, Earth Planet. Sci. Lett., 188, 441-458, 2001.

Schaltegger, U. and Corfu, F.: The age and source of late Hercynian magmatism in the Central Alps - Evidence from precise U-Pb ages and initial Hf isotopes, Contributions to Mineralogy and Petrology, 111, 329-344, 10.1007/bf00311195, 1992.

Schick, H. L.: A Thermodynamic Analysis of the High-temperature Vaporization Properties of Silica, Chemical Reviews, 60, 331-362, 10.1021/cr60206a002, 1960.

Schmidt, A., Nowaczyk, N., Kampf, H., Schuller, I., Flechsig, C., and Jahr, T.: Origin of magnetic anomalies in the large Ebersbrunn diatreme, W Saxony, Germany, Bulletin of Volcanology, 75, 10.1007/s00445-013-0766-6, 2013.

Soppera, N., Bossant, M., and Dupont, E.: Janis 4: An improved version of the NEA Java-based Nuclear Date Information System, Nuclear Data Sheets, 120, 294-296, http://dx.doi.org/10.1016/j.nds.2014.07.071, 2014.

Stone, J. O., Evans, N. J., Fifield, L. K., Allan, G. L., and Cresswell, R. G.: Cosmogenic chlorine-36 production in calcite by muons, Geochim. Cosmochim. Acta, 62, 433-454, 1998.

Strashnov, I. and Gilmour, J. D.: Kr-81-Kr cosmic ray exposure ages of individual chondrules from Allegan, Meteoritics & Planetary Science, 48, 2430-2440, 10.1111/maps.12228, 2013.

Struck, M., Jansen, J. D., Fujioka, T., Codilean, A. T., Fink, D., Egholm, D. L., Fülöp, R.-H., Wilcken, K. M., and Kotevski, S.: Soil production and transport on postorogenic desert hillslopes quantified with 10Be and 26Al, GSA Bulletin, 130, 1017-1040, 10.1130/b31767.1, 2018a.

Struck, M., Jansen, J. D., Fujioka, T., Codilean, A. T., Fink, D., Fülöp, R. H., Wilcken, K. M., Price, D. M., Kotevski, S., Fifield, L. K., and Chappell, J.: Tracking the 10Be-26Al source-area signal in sediment-routing systems of arid central Australia, Earth Surf. Dynam., 6, 329-349, 10.5194/esurf-6-329-2018, 2018b.

Sturchio, N. C., Du, X., Purtschert, R., Lehmann, B. E., Sultan, M., Patterson, L. J., Lu, Z. T., Muller, P., Bigler, T., Bailey, K., O'Connor, T. P., Young, L., Lorenzo, R., Becker, R., El Alfy, Z., El Kaliouby, B., Dawood, Y., and Abdallah, A. M. A.: One million year old groundwater in the Sahara revealed by krypton-81 and chlorine-36, Geophysical Research Letters, 31, 10.1029/2003gl019234, 2004.

Taylor, S. R. and McLennan, S. M.: The continental crust: its composition and evolution, Geoscience Texts, Blackwell, Oxford1985.

Teiber, H., Scharrer, M., Marks, M. A. W., Arzamastsev, A. A., Wenzel, T., and Markl, G.: Equilibrium partitioning and subsequent re-distribution of halogens among apatite-biotite-amphibole assemblages from mantle-derived plutonic rocks: Complexities revealed, Lithos, 220, 221-237, 10.1016/j.lithos.2015.02.015, 2015.

Trieloff, M., Kunz, J., Clague, D. A., Harrison, D., and Allegre, C. J.: The nature of pristine noble gases in mantle plumes, Science, 288, 1036-1038, 10.1126/science.288.5468.1036, 2000.

Uppala, S. M., KÅllberg, P. W., Simmons, A. J., Andrae, U., Bechtold, V. D. C., Fiorino, M., Gibson, J. K., Haseler, J., Hernandez, A., Kelly, G. A., Li, X., Onogi, K., Saarinen, S., Sokka, N., Allan, R. P., Andersson, E., Arpe, K., Balmaseda, M. A., Beljaars, A. C. M., Berg, L. V. D., Bidlot, J., Bormann, N., Caires, S., Chevallier, F., Dethof, A., Dragosavac, M., Fisher, M., Fuentes, M., Hagemann, S., Hólm, E., Hoskins, B. J., Isaksen, L., Janssen, P. A. E. M., Jenne, R., Mcnally, A. P., Mahfouf, J.-F., Morcrette, J.-J., Rayner, N. A., Saunders, R. W., Simon, P., Sterl, A., Trenberth, K. E., Untch, A., Vasiljevic, D., Viterbo, P., and Woollen, J.: The ERA-40 re-analysis, Quarterly Journal of the Royal Meteorological Society, 131, 2961-3012, https://doi.org/10.1256/qj.04.176, 2005.

1151 von Egidy, T. and Hartmann, F. J.: Average muonic coulomb capture probabilities for
1152 65 elements, Physical Review A, 26, 2355-2360, 10.1103/PhysRevA.26.2355, 1982.
1153 Wirsig, C., Zasadni, J., Ivy-Ochs, S., Christl, M., Kober, F., and Schluchter, C.: A
1154 deglaciation model of the Oberhasli, Switzerland, Journal of Quaternary Science, 31,
1155 46-59, 10.1002/jqs.2831, 2016.
1156 Woodhead, J. D. and Hergt, J. M.: A preliminary appraisal of seven natural zircon
1157 reference materials for in situ Hf isotope determination, Geostandards and
1158 Geoanalytical Research, 29, 183-195, 10.1111/j.1751-908X.2005.tb00891.x, 2005.
1159 Wyttenbach, A., Baertschi, P., Bajo, S., Hadermann, J., Junker, K., Katcoff, S.,
1160 Hermes, E. A., and Pruys, H. S.: Probabilites of muon induced nuclear-reactions
1161 involving charged-particle emission, Nuclear Physics A, 294, 278-292, 10.1016/0375-
1162 9474(78)90218-x, 1978.
1163 Zimmermann, L., Avice, G., Blard, P.-H., Marty, B., Füri, E., and Burnard, P. G.: A
1164 new all-metal induction furnace for noble gas extraction, Chemical Geology, 480, 86-
1165 92, https://doi.org/10.1016/j.chemgeo.2017.09.018, 2018.

1166